University of Nebraska - Lincoln

DigitalCommons@University of Nebraska - Lincoln

Mechanical (and Materials) Engineering -- Dissertations, Theses, and Student Research

Mechanical & Materials Engineering, Department of

Winter 12-3-2013

Nd-Fe-B Nanoparticles through Surfactant Assisted Mechanical Milling and Alloy Design

Jordann M. Bornhoft
University of Nebraska-Lincoln, jmbornhoft@huskers.unl.edu

Follow this and additional works at: https://digitalcommons.unl.edu/mechengdiss

 Part of the Materials Science and Engineering Commons, and the Mechanical Engineering Commons

Bornhoft, Jordann M., "Nd-Fe-B Nanoparticles through Surfactant Assisted Mechanical Milling and Alloy Design" (2013). *Mechanical (and Materials) Engineering -- Dissertations, Theses, and Student Research*. 62.
https://digitalcommons.unl.edu/mechengdiss/62

This Article is brought to you for free and open access by the Mechanical & Materials Engineering, Department of at DigitalCommons@University of Nebraska - Lincoln. It has been accepted for inclusion in Mechanical (and Materials) Engineering -- Dissertations, Theses, and Student Research by an authorized administrator of DigitalCommons@University of Nebraska - Lincoln.

Nd-Fe-B Nanoparticles through Surfactant Assisted Mechanical Milling and Alloy Design

by

Jordann M. Bornhoft

A THESIS

Presented to the Faculty of

The Graduate College at the University of Nebraska

In Partial Fulfillment of Requirements

For the Degree of Master of Science

Major: Mechanical Engineering and Applied Mechanics

Under the Supervision of Professor Jeffrey E. Shield

Lincoln, Nebraska

December, 2013

Nd-Fe-B Nanoparticles through Surfactant Assisted Mechanical Milling and Alloy Design

Jordann Meredith Bornhoft, M.S.

University of Nebraska, 2013

Adviser: Jeffrey E. Shield

Surfactant-assisted mechanical milling has been used to produce discrete nanoparticles of both Nd-Fe-B and Sm-Co amenable for bottom-up production of nanostructured or nanocomposite permanent magnets. However, in Nd-Fe-B the comminution of the material proceeds by transgranular fracture, which influences both the morphology of the nanoparticles and the magnetic properties. This paper utilizes alloy design to alter the fracture behavior from transgranular fracture to intergranular fracture. Nd-rich $Nd_2Fe_{14}B$ alloys were produced by melt spinning in an overquenched state. The melt spun ribbons were annealed at 700°C and 800°C to ensure complete crystallization and to form different grain sizes. The resultant materials were then milled using a SPEX8000 mixer/mill with Oleic Acid as a surfactant for varying lengths of time. A second set of alloys was made with a 1 % S (atomic) addition, with the objective to embrittle the grain boundaries and force intergranular fracture. The coercivity decreased with increasing milling time for both S-less and S-containing alloys, from approximately 18 kOe to 3 kOe. The particle refinement process was also dependent on alloy composition, with the S-containing alloy showing a greater propensity for refinement.

Acknowledgements

First and foremost I would like to thank Dr. Jeff Shield, my advisor, for giving me the opportunity to conduct this research. Working within his group has been an honor and privilege and everyday was a new learning experience. My time, knowledge gained, and experiences within his group will go unmatched and I am truly thankful for being selected to work on this project.

Next I would like to thank my research colleagues in our group and those from the NCMN facilities. You have all helped me so much in my time here. We have built some great friendships and had many fun times and I am extremely grateful for those. I would not have been able to conduct successful research without you all.

I would also like to thank the rest of my committee: Dr. George Gogos and Dr. Lucia Fernandez-Ballester for taking the time to learn about my research. As well as the Army Research Office and the Department of Energy- ARPA-E for funding this research. And the Nebraska Center for Materials and Nanoscience Facilities for allowing me the use of their equipment and knowledge. Lastly, I would like to thank my friends and family who have stood by me throughout my academic career.

Table of Contents

List of Tables

List of Figures

Chapter 1 Introduction

1.1 Background

Throughout the ages mankind has been able to utilize natural resources as means of energy; historically these resources have primarily been oil-based fuels. However, in more recent history, lack of ability to attain these resources easily due to political and economic instability, as well as an increasing knowledge of the negative effects these resources have on the environment, has led to a push for more clean, renewable and more efficient forms of energy. Since this push magnetic materials have become a leading resource in the energy industry. Magnets are utilized in many different applications, including electric power generation, motor vehicles, computer hardware, wind turbines, linear actuators, speakers, microphone assemblies, DC motors and automotive starters, and countless more [1]. With unlimited applications magnetic materials have immense potential to make an impact on the energy industry and this potential will continue to grow. Due to this a vast amount of research has gone into maximizing the properties of magnetic materials into broadening the scope of their usage.

Of all the different types of magnetic materials known to man today, the rare-earth permanent magnets top the lists in energy density. The strongest magnet by far is the NdFeB magnet; it has a unique structure that gives it unparalleled magnetic performance. Figure 1.1 illustrates the historical strength of various magnets as a function of time. It is clear to see that NdFeB is almost twice as “strong” (has twice the energy product) as any other magnet currently known. Also depicted in figure 1.1 is the relative volume for same

amount of energy output for several different types of magnets. NdFeB has a lot of energy in a small volume, which is an advantageous quality in many engineering applications, especially miniturazation.

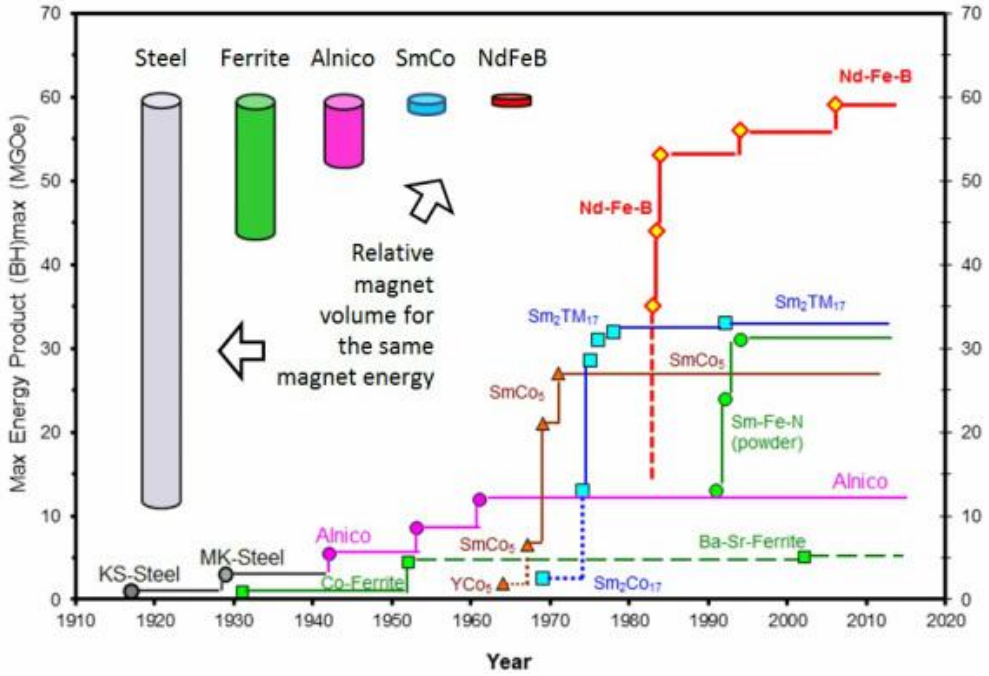

Figure 1.1: History of magnetism and comparative sizes of magnets with equal strength [2].

Nd has one of the larger magnetic moments of all the rare-earths due to its strong outer 4f shell anisotropy, and Fe has the largest magnetic moment when it forms ferromagnetic intermetallic compounds with the rare-earths. This combination of elements gives the NdFeB magnet properties that are almost impossible to mimic [3]. Both materials are quite abundant and therefore have become widely used since NdFeB's discovery in the 1980's. In fact, in 2010 it was estimated that the market for permanent magnets was greater than $11 billion dollars and 65% of that market was attributed to the rare-earth magnets [4].

Clearly there is an expanding demand for these magnets but the cost is also rising. The price of neodymium increased from $17 to $85 per kilogram in 2010 alone, and the cost is continuing to increase [5]. This is because China owns approximately 95% of the 96,000 tonnes of Neodymium produced each year and they have put strict limits on exports. As technology advances so does the demand for NdFeB. In the past 30 years demand for these magnets has gone from 30,000 tonnes annually to 120,000 tonnes annually, and it is estimated that by 2015 the demand will be close to 200,000 tonnes [5]. The demand is continually rising but so is the cost and availability is decreasing. This is where engineering innovation is needed. There is now a greater need for magnetic materials with high energy capabilities but low cost. This has motivated a vast amount of research to answer the question "How can magnets with the same capabilities as the rare-earth permanent magnets be made but at a lower cost?" as the driving force.

1.2 Fundamentals of Magnetism

The sources of magnetic fields are electric currents and magnetized materials. The most fundamental magnetic quantity is the magnetic dipole moment; m. The magnetic moment is associated with the spin of the electron and its orbit around the nucleus (figure 1.2). The fundamental moment is easy to calculate utilizing equation 1.1 [6].

$$m = \frac{-e}{2m_e} L \qquad \text{Eqn. 1.1}$$

where e is the unit of elementary charge, L is the angular momentum (either from the spin or orbital rotation), and m_e is the mass of an electron. In most materials the sum of the magnetic moments is zero, but in magnetic materials there is a resultant moment on the atomic scale which results in magnetization [6].

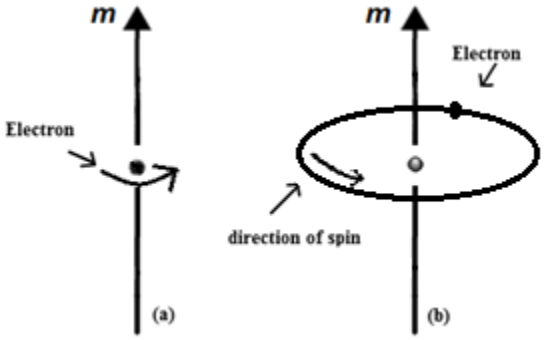

Figure 1.2: a) Magnetism caused by spin moment. b) Magnetism caused by orbital moment.

1.3 Types of Magnetism

While there are many types of magnetization, five main types will be discussed: diamagnetism, paramagnetism, ferromagnetism, ferrimagnetism, and antiferromagnetism.

In all materials there is a tendency to oppose an applied magnetic field; this is called diamagnetism. When this is the only contribution to the overall magnetism of the material, the material is said to be diamagnetic. In this type of material there are no unpaired inner shell electrons, so the effect is usually quite weak [7]. When a material contains unpaired electrons it is said to be paramagnetic. The unpaired electron is able to align its magnetic moment in any direction, allowing the moments to align themselves with an external field. Both diamagnetism and paramagnetism require an eternally

applied field in order to exhibit magnetic behavior. Ferromagnetism and ferrimagnetism are both able exhibit magnetic behavior in the absence of an external applied field.

In ferromagnetic materials there is a tendency for the magnetic moments to orient themselves parallel to each other in addition to an external field. The moments will remain parallel to each other even when the external field is no longer applied. This tends to be a strong effect and ferromagnetic materials have magnetic properties that are easily detectable [8]. Magnetic domains are present in ferromagnetic materials. A magnetic domain is simply a physical region of the material that has uniform magnetization. In a magnetic domain all the individual magnetic moments are aligned. A material can have many domains or one domain. Like ferromagnetic materials, ferrimagnetic materials are also able to retain magnetization in the absence of an external field. But in ferrimagnets the neighboring electrons tend to align themselves in opposite directions; however the magnetic moments of the two atoms are unequal, which allows there to be a net magnetization [6].

Unlike both ferromagnets and ferrimagnets, antiferromagnets are not able to retain magnetization in the absence of an external field. This is because the neighboring electrons have a tendency to align themselves in opposite directions and their magnetic moments are equivalent. These materials have zero net magnetization [6]. Figure 1.3 illustrates the electron alignment of all these materials.

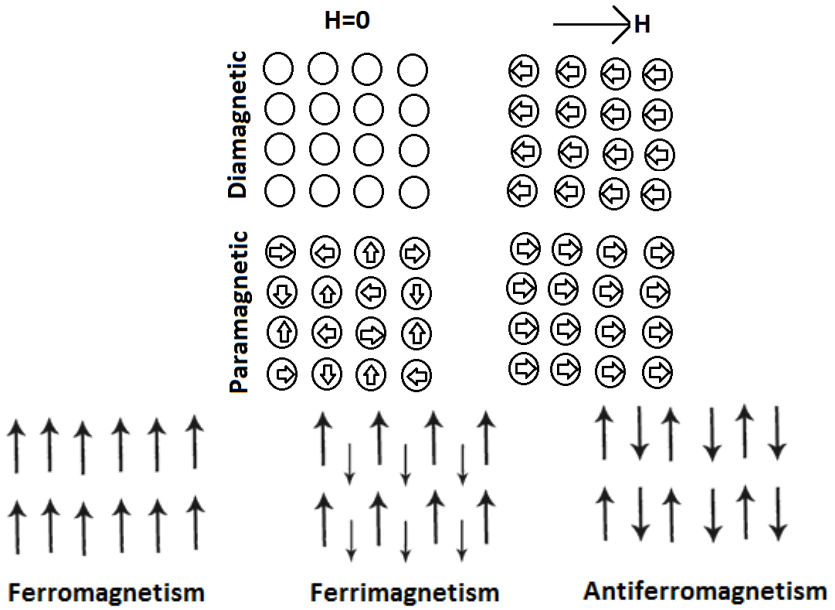

Figure 1.3: Electron alignments of diamagnets, paramagnets, ferromagnets, ferrimagnets, and antiferromagnets.

1.4 Magnetism and Hysteresis

A characteristic of any ferromagnetic material is the irreversible nonlinear response of its magnetization (M) to an externally imposed magnetic field (H) [6]. In this research the type of magnetization measured was the mass magnetization; this is the magnetic moment divided by the total mass and is measured in emu/g. The magnetic field (H) is measured in Oersteds (Oe). This response can be seen in the hysteresis loop (figure 1.4).

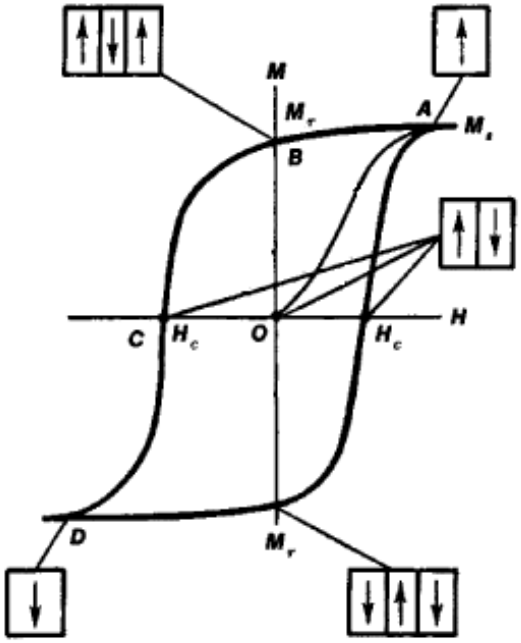

Figure 1.4: Typical hysteresis loop. A) The saturation magnetization(M_s) B) The remanence (M_r) C) The coercivity (H_c) D) return to saturation magnetization in the reversed field [After 9].

Starting at the origin (O) the magnet has no net magnetization and has experienced no applied magnetic field. This is illustrated by the arrows in the box corresponding to point O. There are an equal number of up arrows as down arrows (the arrows represent magnetic domains), so there is zero magnetization. Once a field is applied the domains begin to align in the direction of the field and magnetization occurs. At point A, all the moments are aligned in the same direction, the curve plateaus, and this is known as the saturation magnetization. No matter how much additional field is applied the magnet will never gain more magnetization then this value.

The field then begins to reverse and at point B there is no magnetic field being applied to the magnet but the magnet retains some magnetization. This is known as the

remanence (M_r), or the measure of the remaining magnetization when the driving field is reduced to zero. Eventually point C is reached where for a certain opposing field the magnetization reaches zero. This is known as the coercivity (H_c) of the magnet, the measure of the reverse field needed to drive the magnetization to zero after being saturated. Once the field is fully reversed, at point D, the magnet will again experience saturation magnetization in the opposite direction. You can then begin to apply the field in the original direction and reverse the loop back to point A. However, this hysteresis loop describes a material with many domains. A material with a single domain acts in a slight different manner.

Single-domain materials follow the Stoner-Wohlfarth model. It is the simplest model to exhibit hysteresis. A Stoner-Wohlfarth particle (figure 1.5) has uniform magnetization with a magnetocrystalline origin in an applied field at an angle α to the anisotropy axis.

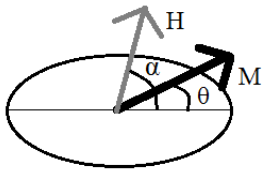

Figure 1.5: A Stoner-Wohlfarth particle, where H is the applied field and M is the magnetization.

In the Stoner-Wohlfarth model, the hysteresis response is dependent on the angle of the applied field, α. The dependency of the hysteresis loop on this angle is shown in figure 1.6. When α is equal to zero, the hysteresis loop is considered ideal, and it has maximum M_r and maximum H_c. The worst case scenario is when α is 90°, this results is zero M_r and zero H_c [6].

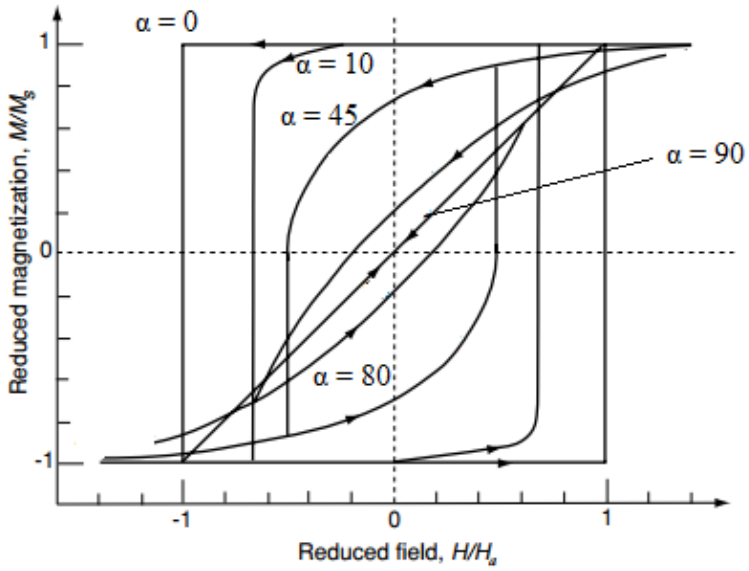

Figure 1.6: Hysteresis loops for the Stoner-Wohlfarth model for various angles α after [6].

When you have a randomly oriented array of Stoner-Wohlfarth particles, the model allows for the prediction of the magnetic properties on the hysteresis loop (Figure 1.7). This model can be utilized when examining single domain particles in ferromagnets.

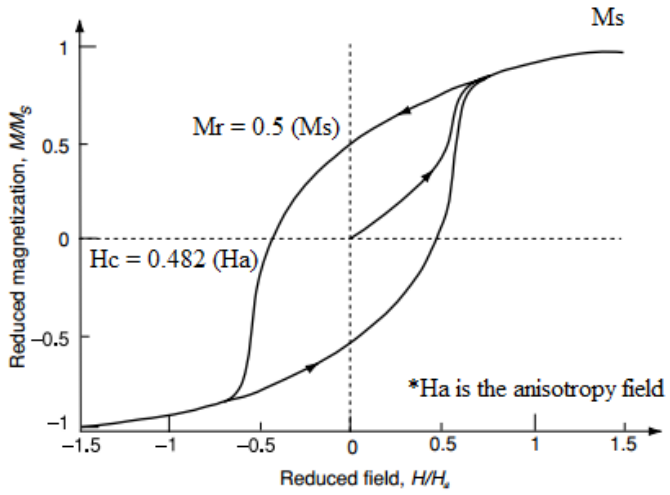

Figure 1.7: Hysteresis loop for an array of randomly oriented Stoner-Wohlfarth particles [after 6].

1.5 Intrinsic and Extrinsic Properties

Contained within the hysteresis loop are both intrinsic and extrinsic properties. The saturation magnetization is the sole intrinsic property within the loop. It is dependent on the particular material and exists within the domain of a ferromagnets; this cannot be manipulated except through site substitution in the structure [6].

The extrinsic properties include the coercivity and the remanence. These are dependent on a variety of variables including sample shape, thermal history, grain size, defects, surface roughness and more. Because these properties can be manipulated, their optimization can create a better performing magnet. Anisotropy plays an important role in the optimization of coercivity. Magnetocrystalline anisotropy is when the atomic structure of the material introduces preferential directions for magnetization which plays a role in the coercivity and the remanence. Other types of anisotropy include shape and stress, although magnetocrystalline can be the strongest.

1.6 Energy Products

The energy product or $(BH)_{max}$ is the merit of strength for a permanent magnet. The larger the energy product is the stronger the magnet will be. When determining the energy product a B H curve must be utilized. This graph can be derived from the hysteresis loop. The H field runs along the x-axis and is the applied field. The magnetization on hysteresis loop is converted to the B field and along the y axis. The conversion is illustrated in Eqn. 1.2.

$$B = 4\pi M + H \qquad \text{Eqn. 1.2}$$

where M is the volume magnetization and H is the magnetic field strength. The $(BH)_{max}$ is the largest rectangle within the second quadrant of the B H curve (fig 1.8). In order to maximize this product one can work to maximize both the remanence and the coercivity.

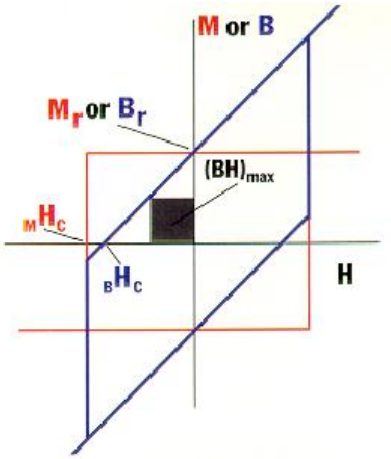

Figure 1.8: BH Graph derived from the MH graph. The shaded region is the energy product [10].

1.6 Classifications of Magnets

Magnetic Materials can be characterized under two groups: soft magnets and hard magnets. Soft magnets are characterized by their low coercivity (< 25 Oe) and narrow hysteresis loop (small $(BH)_{max}$), while hard magnets are characterized by their high coercivities (> 2 kOe) and wide hysteresis loops (large $(BH)_{max}$). These are illustrated in figure 1.9.

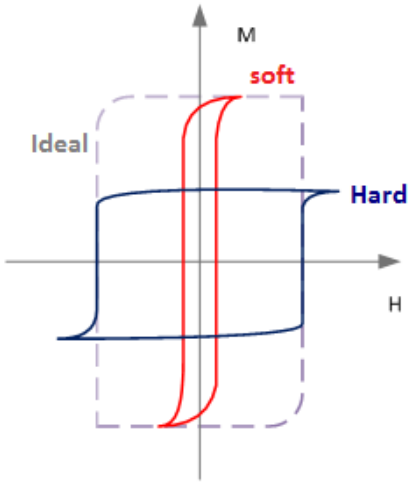

Figure 1.9: Hysteresis loop of a soft magnet, a hard magnet, and an ideal magnet is shown by the dashed lines.

The term permanent magnet is given to any magnet that has a remanence value, i.e. it has the ability to maintain magnetization when the field is no longer applied. Rare-earth permanent magnets are all hard magnets because they are used in a permanently magnetized state (i.e no reversal). These coercivities are a result of the microstructure of the material. The rare-earth permanent magnets have the microstructure needed for extremely high coercivities and energy products.

Chapter 2 Literature Review

2.1 Nanocomposite Permanent Magnets

There are many different approaches of how to develop more effective and efficient permanent magnets currently being evaluated. The following is a topical review with advancements in research specific to NdFeB magnets.

One approach to developing magnets with extremely high energy products is by forming a composite magnet with a soft and hard phase, or a two-phase magnet. Skomski et al [11] predicted that the exchange hardening of two-phase nanostructured magnets that consisted of a soft phase with a high magnetization and an aligned hard phase (with a rare-earth content of only 5%) could achieve extremely high energy products. Specifically, a multilayered magnet with alternating layers of $Sm_2Fe_{17}N_3$ and $Fe_{65}Co_{35}$ could achieve an energy product of 120 MGOe [11]. It was also determined that the energy product of these two-phase magnets was larger than the corresponding rare-earth intermetallics alone [11]. This is due to optimum exchange coupling between the hard and soft phases of the magnets which occurs on the nanoscale. Exchange coupling is simply the way the phases interact with one another. Good exchange coupling, or interactions, can optimize the magnetic performance. These exchanges occur between single domain particles, for which there is critical maximum radius that a single domain can occur. Above this radius it is more energetically favorable to form multiple domains. So formation of nanopartcicles below this radius is necessary for optimum magnetic properties. For NdFeB the single domain radius is 220 nm [6].The formula for the single domain radius is shown in equation 2.1, and the single domain radius depends upon the

exchange stiffness (A), the anisotropy constant (K), the permeability of free space (μ_0), the saturization magnetization (M_s).

$$R_{SD} = \frac{36\sqrt{AK_1}}{\mu_0 M_s^2} \qquad \text{Eqn. 2.1}$$

Also important in a nanocomposite is the length scale, which is the length over which the exchange coupling occurs. This corresponds to twice the domain wall width, 2δ, where:

$$\delta = \pi\sqrt{\frac{A}{K}} \qquad \text{Eqn. 2.2}$$

For typical hard phase parameters A and K, δ is few nanometers. Thus the scale of the soft phase must be approximately 10 nm for optimum exchange coupling.

Fischer et al [12] also used numerical micromagnetic calculations using finite element techniques to analyze composite rare-earth magnets. It was found that in isotropic $Nd_2Fe_{14}B$ magnets containing α-Fe, the remanence could be enhanced by up to 60% and the coercivity could be enhanced by up to 30% given an ideal grain size, particle shape, and volume fraction of the phases [12]. Two-phase composite magnets show potential, but the method of processing of the $Nd_2Fe_{14}B$ is also critical in developing effective high-energy magnets.

In order to produce high performance magnets; microstructure, composition and processing are three vital factors. When producing bulk $Nd_2Fe_{14}B$ magnets there are three

common fabrication methods including sintering, hot deformation, and polymer bonding. Sintered magnets tend to be of full density, anisotropic, have comparatively uncomplicated shape and have energy products in the range of 30-50 MGOe. Magnets processed through hot deformation have full density, can have isotropic or anisotropic properties, can be formed into various shapes, and have energy products in the order of 15-46 MGOe. Polymer bonded magnets have lower density than the other two methods, are typically isotropic, can have complex net-shapes, and energy products in the range of 10-18 MGOe [13]. Depending on the application and desired properties of the magnet an appropriate processing technique would be selected. When producing nanocomposites these bulk approaches are not necessarily appropriate. They could be used as a secondary treatment to produce a nanocomposite bulk magnet consisting of a rare-earth phase and a transition metal phase. When fabricating the nanoparticles of NdFeB, different processing techniques such as rapid solidification and milling are implemented. These techniques produce an isotropic product while these heat treatments allow for an anisotropic product.

Rapid solidification is another processing technique commonly used when making $Nd_2Fe_{14}B$ magnets with high energy products. Pinkerton et al [14] analyzed the properties of rapidly solidified $Nd_2Fe_{14}B$ via melt spinning. They found that the melt spun ribbons were magnetically isotropic and had a coercivity of up to 15 kOe and a remanence 8kG. In these ribbons the small grain size was critical to magnetization reversal. They found the grains to be of "single domain". Domain-wall formation and propagation through single grains was the mechanism responsible for both the magnetization and demagnetization. Coehoorn et al [15] was able to attain a novel type of magnetic material

via melt spinning and annealing. Utilizing an initial composition of $Nd_4Fe_{78}B_{18}$ ingot and melt spinning to acquire amorphous flakes, they then were able to anneal the material in two steps. First the Fe_3B phase crystallizes at a lower temperature and then the $Nd_2Fe_{14}B$ magnetic phase was formed at a higher annealing temperature. The exchange interactions between the two phases lead to an increase in remanence. While only 15% of the alloy was the hard magnetic phase, they were still able to achieve energy products as high as 11.9 MGOe.

More recently the effect of Nd content on the magnetic properties of melt spun ribbons has been analyzed. Manaf et al [16] was able to show that there are three main categories of isotropic melt spun NdFeB alloys. Those categories are a) near stoichiometric when the Nd content was between 11-13% b) low Nd when the Nd content was between 8-11% and c) high Nd when the Nd content was greater than 13%. The near-stoichiometric alloys have wide exchange coupling between the $Nd_2Fe_{14}B$ grains and therefore they have a high remanent polarization. The low Nd alloys have added coupling between the $Nd_2Fe_{14}B$ and α-Fe phase so they have even higher remanent polarization. However, although the remanent polarization increases there is decrease in coercivity. Ahmad et al [17] analyzed the properties of the Nd-rich alloys and found that with a Nd content between 13%-15% the coercivity increased from 0.9 to 1.56 kOe. And upon further addition of Nd the coercivity continued to gradually increase up to 1.8 kOe. However, the increase in coercivity was matched with a decrease in remanent polarization. Therefore, Nd-rich $Nd_2Fe_{14}B$ have greater coercivities than the $Nd_2Fe_{14}B$ phase alone.

Another important aspect of designing more efficient $Nd_2Fe_{14}B$ magnets is the effect of grain size on the magnetic properties. An extensive amount of research has been conducted concerning this issue. Fischer et al [18] analyzed this in nanocrystalline ferromagnetic materials, specifically $Nd_2Fe_{14}B$ and α-Fe nanocomposite magnets, using micromagnetic calculations finite element techniques. As already noted in this two-phase composite magnet the α-Fe phase is responsible for a large spontaneous magnetization and the $Nd_2Fe_{14}B$ phase is responsible for the high coercivity when the phases are exchanged coupled. The analysis indicated that the optimal microstructure for a composite magnet containing these materials was having hard magnetic grains with a mean diameter of 20 nm and soft grains with a mean diameter of 10 nm. The optimal volume of the soft phase was determined to be 40%. In general the study predicted that as grain size decreased there would be a decrease in coercivity and an increase in remanence. Betancourt et al [19] analyzed this experimentally and their results were in agreement with the predictions. However, they found that in composites containing below 20% of the α-Fe phase the coercivity did not decrease but stayed constant. Xiao et al [20] was also able to experimentally determine the critical grain size of the soft phase to be less than 20 nm. Experimentally they showed that in the composites where the soft phase had grains larger than this value, then they began to become decoupled and showed a decrease in coercivity.

Another processing technique of rare-earth permanent magnets is high energy ball milling (HEBM). Harada et al [21] used mechanical grinding to reduce the particle size to 1 μm but found that additional grinding did not result in a further reduction of particle

size. HEBM gives rise to several issues when attempting to develop nanoparticles. It leads to a wide size distribution, the grains become randomly oriented and more amorphous resulting in a loss of magnetic properties, and the particles re-weld together during the process. In an attempt to further reduce the particle size using HEBM, research began on surfactant-assisted mechanical milling (SA-HEBM). The surfactant aids in the prevention of the re-welding of the particles, and can act as a lubricant to reduce potential contamination. Nanoparticles of SmCo-type alloys were successfully fabricated using surfactant-assisted HEBM and an increase in magnetic properties was achieved [22, 23]. Nd-Fe-B chip-like nanocrystals and nanoflakes with strong magnetocrystalline anisotropy have also been produced via SA-HEBM utilizing a field during the milling process and two-stage HEBM process, respectively [24, 25, 26]. Even though nanoparticles have been produced, the grains experienced transgranular fracture during the HEBM process [27], and this greatly affects both the morphology and the magnetic properties. Transgranular fracture produces polycrystalline particles that have multiple magnetic domains from re-welding, resulting in an isotropic product with a diminished energy product.

In summary, the main problems when attempting to produce nanoparticles via HEBM include the re-welding of the particles and transgranular fracture producing polycrystalline particles. While using a surfactant has been proven to aid in the prevention of the re-welding of the particles, there has yet to be a method of preventing the transgranular fracture seen in HEBM. If the grains were to fracture along the grain boundaries, that is they experience intergranular fracture, then the resulting nanoparticles

would be single crystalline and could be aligned with a field to produce higher energy products than seen in previous research.

2.2 Objectives

SA-HEBM already shows promise in developing Nd-Fe-B nanoparticles which can be utilized in bottom-up production of nanocomposite permanent magnets. In this project, we will seek to control nanoparticle formation during surfactant-assisted high energy ball milling by altering the fracture mechanics. Through alloy design, the transgranular fracture dominant in previous studies on $Nd_2Fe_{14}B$ can be changed to intergranular fracture as shown in Figure 2.2.

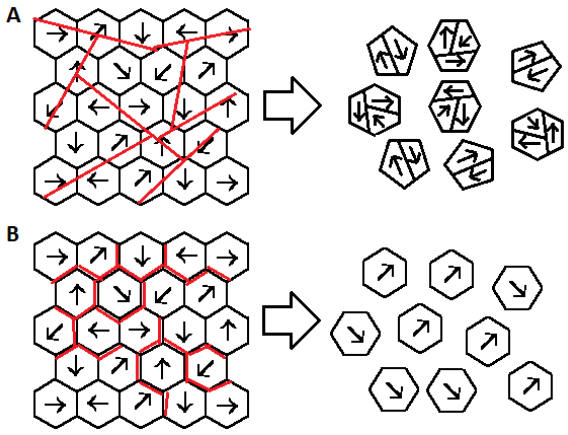

Figure 2.1: A) Transgranular fracture produces polycrystalline particles. B) Intergranular fracture produces single-crystalline particles.

Furthermore, the introduction of sulfur as an embrittlement agent can further promote intergranular fracture and embrittle the grain boundary regions, making nanoparticle formation easier and with less energy. It is known that Neodymium segregates to the grain boundaries in Neo-rich samples [16, 17]. When S and Nd react they tend to form NdS or Nd_2S_3, which is very brittle. Moreover, S tends to embrittle metal alloys. This

will aid in the fabrication of single-grain and single magnetic domain nanoparticles. Production of single domain nanoparticles is critical to the advancement of rare-earth permanent magnet materials and will allow for further progression in the bottom-up processing of anisotropic exchange coupled nanocomposite magnets.

Chapter 3 Material Properties

3.1 Basic Properties of NdFeB

Neodymium Iron Boron (Nd-Fe-B) magnets have the highest energy products currently attainable. They have extremely high coercivities while maintaining good remanence, this is largely due to their unique crystallographic structure. The phase of NdFeB that produces the record high energy products has a tetragonal structure belonging to the $P4_2/mnm$ space group [28]. The unit cell is very complex and contains 68 atoms (Figure 3.1).

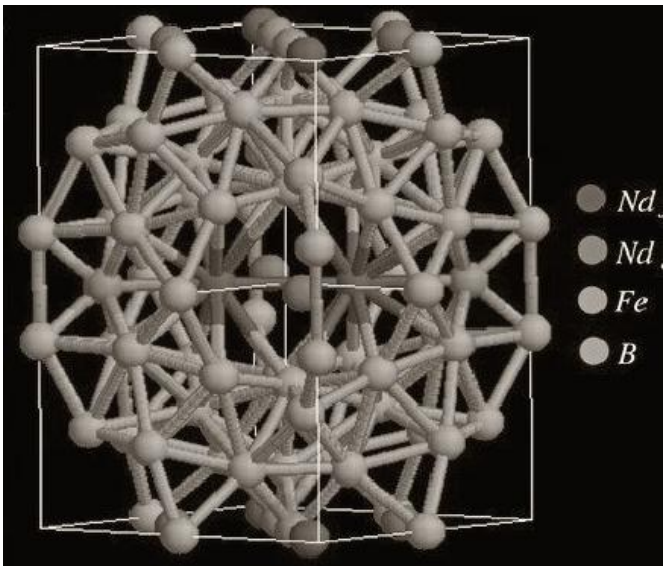

Figure 3.1: Unit Cell for NdFeB after [30]. It contains six Fe sites, two Nd sites, and one B site.

This structure consists of several layers. There are Fe layers in which almost all of the Fe atoms are located. There are also Nd-rich layers, where all of the B atoms are located. The Nd-rich layers are separated from one another by the Fe layers and are the reason for the magnetic properties. It is this structural feature that gives the $Nd_2Fe_{14}B$ a

high degree of magnetocrystalline anisotropy [29]. In order to get the best magnetic properties one must achieve the $Nd_2Fe_{14}B$ phase. Figure 3.2 below shows the phase diagram for the ternary alloy. To achieve solely the T1 phase ($Nd_2Fe_{14}B$), one must hit the peritectic point outlined in the red dashed line.

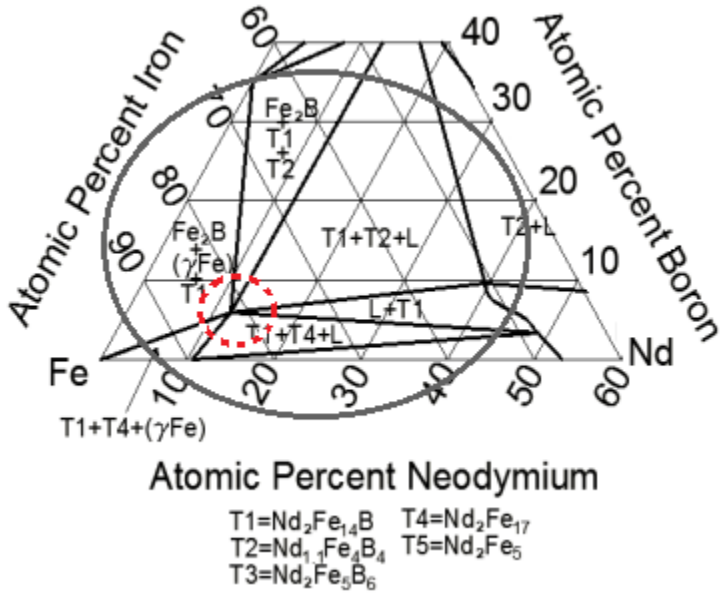

Figure 3.2: Phase Diagram for NdFeB after [31]

3.2 Nanocomposite Magnets

While $Nd_2Fe_{14}B$ is currently the strongest permanent magnet with a theoretical energy product of 64 MGOe for anisotropic materials, there is always motivation to develop materials with higher energy products. Hard magnets have high coercivities while soft magnets that contain elements like Fe have high a remanence. One way to take advantage of both materials is to combine them in a composite material. Pairing these hard/soft phases together allows for both high coercivity and high magnetization resulting in much higher energy products. To fully take advantage of the exchange interactions

(aka exchange coupling) between the two materials, the phases must be assembled in the nanoscale. Pairing the hard phase of $Nd_2Fe_{14}B$ (with a very high coercivty) with a soft phase of FeCo (with a very high magnetization) would result in a nanocomposite material with higher energy product than that of a single phase $Nd_2Fe_{14}B$ material. The first step in the development of nanocomposites is the fabrication of single domain nanoparticles. Fabrication of both the hard and soft phase nanoparticles, without reducing their magnetic properties, must be achieved. As stated in the objectives, the proposed method of forming such particles is by altering the fracture mechanism and adding Sulfur as an embrittlement agent. The hard phase nanoparticles must then be aligned and arranged for the optimum exchange coupling. Finally, they must be consolidated into a final nanocomposite material (Figure 3.3). Forming these nanophases and processing them in bulk is the challenge when attempting to produce nanocomposites with extremely high energy products [32].

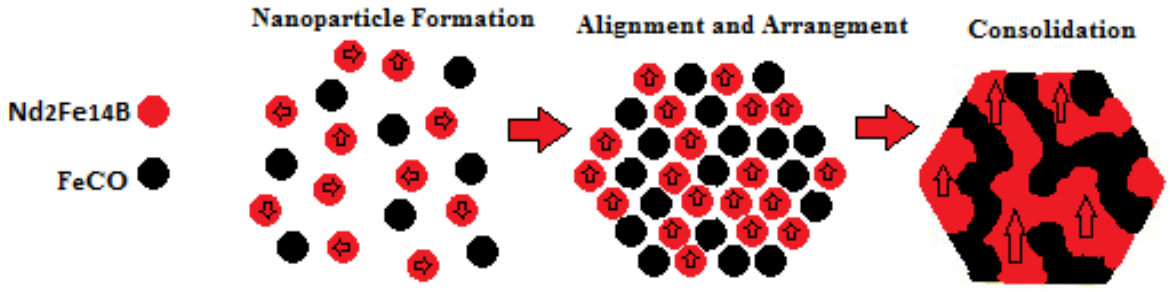

Figure 3.3: Nanocomposite Formation

Chapter 4 Experimental Procedures

4.1 Sample Preparation

The $Nd_2Fe_{14}B$ magnets were made as Nd-rich samples. So the formula utilized was $Nd_{15}Fe_{77}B_8$ (atomic %). When making the magnets that contain sulfur the following formula was utilized: $(Nd_{15}Fe_{77}B_8)_{99} + S_1$ (atomic %). The atomic percentages were then converted to weight percentages which are shown in the table below.

Table 4.1: Weight Percentages of Samples Prepared

	Nd	**Fe**	**B**	**S**
Neo-Rich Sample	33%	65.6%	1.3%	0%
Sulfur Additive Sample	33.03%	65.65%	1.32%	.01%

These masses were weighed out using a precision scale (error +/- 0.2 mg). The raw materials with the corresponding purities were then placed into an arc melt machine: Nd (99.9%), Fe (99.97%), B (99.5%, S (99.9995%). The smaller pieces (mostly Boron and Sulfur when applicable) were laid underneath the larger pieces (Iron and Neodymium) to prevent them from shifting from the power of the arc melter. The arc melting is carried out in an Argon atmosphere to prevent oxidation. To achieve an Argon atmosphere, the arc melter was evacuated and refilled several times; first to 100, then to 75, then to <60 millitorr. The sample was arc melted, rotated and re-melted to ensure a homogenous mixture. The sample was allowed to fully cool before removal.

The ingot was then cut into smaller pieces using a diamond saw. Those pieces were then placed into a quartz crucible with a 0.5 mm hole for melt spinning. The quartz crucible was placed inside of the melt spin machine, the machine was evacuated three times down to 4.5 10^{-2} torr, 3.5 10^{-2} torr, and 2.3 10^{-2} torr. After each evacuation it was refilled with Argon. Then the ballast is over pressurized by 0.2 bar. The cooling water was turned on and the wheel speed is turned up to 30 m/s. The high voltage was turned on and the melting begun. The sample was allowed to melt for two to three minutes to ensure full homogenization before the ballast was released and the material passed over the wheel, cooling instantly and forming ribbons. The samples were melt spun at a speed of 30 m/s to over-quench them, This allows the ribbons to have extremely small grain size and allowing them to be amorphous samples.

A portion of the sample was separated from the bulk to undergo differential thermal analysis (DTA) to ensure the melt spun sample was in fact amorphous. Differential thermal analysis (DTA) is a process that indentifies exothermic or endothermic changes in a sample by comparing the temperature difference between the sample and a reference sample during a thermal cycle. An exothermic or endothermic reaction indicates a change in crystallization. In this experiment the Perkin Elmer DTA7 was utilized for DTA analysis. Aluminum oxide was used as the reference sample. The samples were heated to 50 °C and held for one minute, then the samples were heated from 50 °C to 750 °C at a rate of 10 °C per minute, they were then cooled back down to 50 °C at a rate of 20 °C per minute. The results of the DTA will be further discussed in Chapter 5.

The next step in the process is to anneal the samples to allow for grain growth and crystallization. The samples were annealed at both 700 °C and 800 °C. To prep for annealing the sample ribbons were crushed using a mortar and pestle, then placed into tantalum foil tubes. These were then placed in SiO_2 tubes which were evacuated to a pressure below 60 millitorr and refilled with Argon a minimum of four times to prevent oxidation, and then they were tube sealed.

After annealing the samples, they were ball milled for varying amounts of time: 15 min, 30 min, 1 hr, 2 hr, 4 hr, and 8 hr. To prepare for milling the samples were placed into a milling vile along with 50% Oleic acid (as the surfactant) and 50% Heptane (as the milling medium). Percentages are by weight. Two balls were also placed into each vile at a 10:1 ball to powder ratio (by mass). The containers were closed in a nitrogen atmosphere glove box to prevent oxidation during milling.

Once milled for the specified time the samples were cleaned of the surfactant and milling medium by rinsing with ethanol. Once rinsed with the ethanol the samples were centrifuged for 15 minutes and the process was repeated 3 times. After being centrifuged three times there was no indication of remaining surfactant. The final cleaned samples were left out to dry overnight and then placed into their testing vials. The samples were labeled as shown in Figure 4.1.

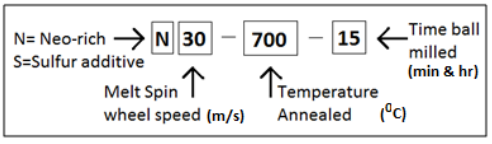

Figure 4.1: Sample Identification. It is important to note that the time milled is labeled 15, 30 for minutes then switches to 1, 2, 4, and so on for hours.

4.2 Sample Characterization

The samples were characterized using several different techniques. How these techniques work and what they were used to characterize is further described in this chapter.

4.2.1 X-Ray Diffraction

X-Ray diffraction is an analytical technique that gives information about the crystallographic structure from which the chemical composition of a material can be identified. To understand how x-ray diffraction enables us to utilize this information we must first look at how the x-ray is produced.

An x-ray tube is used to generate x-rays which are produced when electrons traveling at high speed collide with a metal target. An x-ray tube requires three components: 1) a source of electrons, 2) a high accelerating voltage, and 3) a metal target [33]. The tube contains an anode (metal target) and a cathode (hot filament). A high voltage administered across the tube forces electrons to travel at very high speeds from the cathode to the anode. Once the electrons hit the metal target, x-rays are emitted from the tube at a focal spot via a small window from the tube. A typical X-ray tube is shown in Figure 4.2. The x-ray diffraction machine utilized in this research was a Rigaku Multiflex Diffractometer, which utilizes a copper target and produces CuK_{α} x-rays.

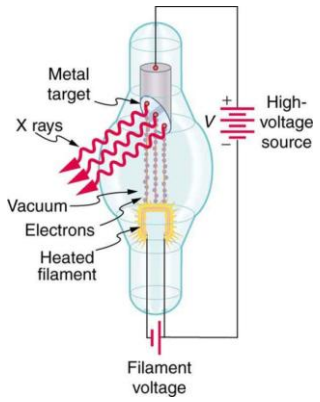

Figure 4.2: Illustration of X-ray tube [34].

Once these X-rays are produced and emitted from the tube, they hit the target material and bounce off the atoms in the sample. If the atoms are arranged in a random orientation the x-rays are scattered randomly, but if the atoms are oriented with periodicity they scatter the x-rays in particular directions described by Bragg's law, shown in equation 4.1.

$$n\lambda = 2dsin(\theta) \qquad \text{Eqn. 4.1}$$

Where n is an integer, λ is the wavelength, d is the interatomic spacing, and θ is the angle between the x-ray and the parallel plane. This relationship is shown in figure 4.3.

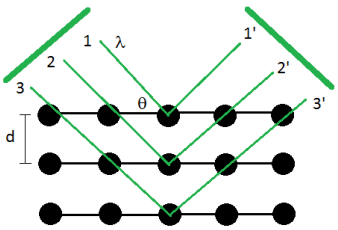

Figure 4.3: Diffraction of x-rays in a crystal lattice according to Bragg's Law.

As the x-rays are bouncing off each atom they are displaced a different amount depending on the atomic spacing and atom location, causing them to become out of phase. This leads to interference either constructive or destructive. In constructive interference the waves are in phase with one another causing the resulting wave to have higher amplitude. In destructive interference the waves are out of phase, resulting in a decreased amplitude. A detector picks up these waves and a diffraction pattern is formed, which is essentially a "finger print" for the material. On this pattern large peaks occur where there is a high intensity of scattered x-rays; these peaks are at locations specific to Bragg's law and unique to particular materials. The diffraction pattern can be indexed to a material and can tell us the lattice configuration.

4.2.2 Scanning Electron Microscope

Scanning electron microscopy is a technique that allows for nanoscale imaging utilizing electrons instead of light. Electron microscopes have many advantages over light microscopes in that they have extremely high resolution and allow the user to see clear images at very high magnifications. The SEM microscope has the ability to yield information about external morphology, orientation, chemical composition and crystalline structure [35].

When using the SEM, data that is collected over a specified surface area and the SEM generates a 3-D image of the spatial variations. To generate this image a beam of high energy electrons are accelerated towards the sample. The electrons carry a large amount of energy and through electron-sample interactions this energy is dissipated,

creating products that are useful to characterize a material. The signals that produce the SEM images are secondary electrons and backscattered electrons [35]. The secondary electrons are critical to show the topology. One advantage of the SEM, is that it does not harm the sample in anyway and is considered to be non-destructive, so you can analyze the same sample multiple times. Figure 4.4 is a schematic of a typical scanning electron microscope.

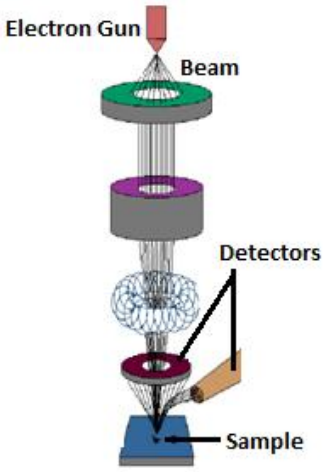

Figure 4.4: Schematic of a scanning electron microscope [36].

Sample preparation for the SEM was as follows. The ribbon samples were hand grinded using a mortar and pestle to produce fresh fracture surfaces and were placed on CU-tape and loaded into the SEM. The powder samples were also placed on CU-tape but the excess powder was removed with an air duster before analysis.

4.2.3 Transmission Electron Microscope

Transmission electron microscopy is similar to scanning electron microscopy in that it also uses electrons to produce an image instead of light. However, instead of the electrons being scattered off the sample, they are actually accelerated through the sample.

The TEM allows for even higher levels of magnification, allowing the viewer to see down to a few angstroms (10^{-10} m) [37]. Figure 4.5 shows a schematic of a transmission electron microscope.

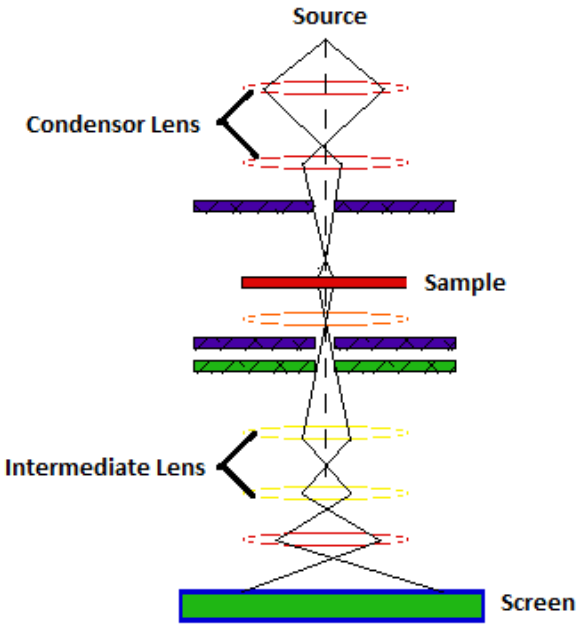

Figure 4.5: Transmission Electron Microscope [38].

Again an electron gun produces a beam of monochromatic electrons. As this beam travels down the column it passes through condensing lenses that focuses the electrons into a small thin coherent beam. These lenses also control the size of the spot as well as the intensity and brightness. Once the electrons hit the specimen, some of them are transmitted through it and it the transmitted portions that are focused by an objective lens into an image. This image is enlarged and can be analyzed by the user [38]. TEM images can even show specific atoms, and are extremely useful for sample characterization.

The TEM requires a specific sample preparation for use. For powder samples, the powder is placed in a heptane solution and is placed into an ultrasonic vibrator for several minutes. This allows for the nanoparticles to become suspended in the solution, while the larger particles descend to the bottom. An eye dropper is then used to pipette out a small volume of the mixture and is placed onto a copper grid. The grid is then allowed to dry and is placed into the TEM for analysis.

4.2.4 Magnetic Property Measurement System

Quantum Design's® Magnetic Property Measurement System (MPMS) is a machine that allows for the characterization of magnetic properties. It is a very sensitive magnetometer that can detect signals as small as 5×10^{-18} emu, has the ability to produce extremely large magnetic fields, and can control the temperature range of samples. The MPMS works by applying a magnetic response to the sample and then measuring the magnetic moments of the sample and from this the coercivity, saturation magnetization, remanence, susceptibility and more can be found. These features make the MPMS a key component in magnetic characterization.

The MPMS is able to detect such small signals due to the fact that it indirectly measures the magnetic response. The system contains several superconducting components including a superconducting magnet and detection coil. The magnet produces the large fields while the coil inductively couples with the sample. It also contains a superconducting quantum interface device (SQUID) which is connected to the detection coil. Lastly it contains a magnetic shield that surrounds the SQUID [39].

The sample moves through several superconducting detection coils connected to the SQUID. This allows the current from the coils to inductively couple to the SQUID sensor. The SQUID produces an output voltage proportional to the current flowing in the SQUID coil; this means it is basically a current-to-voltage convertor.

During the measurement process, the sample moves through the superconducting coils and the magnetic moment of the sample induces an electric current in the detection coils. The SQUID input coil forms a closed superconducting loop with the detection coils and connecting wires. The change in flux in the detection coils produces a change in the current in the detection circuit. This change is proportional to the magnetic flux, which in turn produces change in the SQUID output voltage proportional to the magnetic moment [39]. This system provides the most sensitive measurement capabilities available and it is critical for measuring accurate magnetic properties.

For analysis of the magnetic properties in this experiment, the samples were prepped as follows. For the ribbons, a small section was weighed using a precision scale (+/- .0001 mg), The sample was then taped to a small piece of plastic using nonconductive tape, as to not interfere with the magnetic properties. The plastic was then propped inside a straw and placed into the SQUID for analysis. For the powder samples, again a small amount of powder was weighed using the same precision scale. The powder was then placed into a SQUID capsule and a small amount of superglue was placed on the powder to stabilize it. The capsule was then placed inside of a straw which was then placed into the SQUID for analysis. Several different sequences were used to obtain the data depending on the sample. However, in every sequence the maximum field applied

was 70 kOe, and each sample underwent full reversal (to -70 kOe), in order to obtain data on the saturation magnetization, the remanence and the coercivity. The results of the magnetic data will be further discussed in chapter 5.

Chapter 5 Results

X-ray diffraction patterns were obtained for the N30-AsSpun and S30-AsSpun samples (Figure 5.1). The broad peaks seen in both samples indicate that they are mostly amorphous; however, the large number of sharp peaks indicates that there is some crystallization. To determine the thermal stability, differential thermal analysis (DTA) was conducted on both the samples (Figure 5.1). The exothermic peak in the DTA graph indicates crystallization of the amorphous, consistent with the XRD data. In the N30AsSpun sample the onset temperature of the peak was 560.6 °C, consistent with the crystallization temperature of $Nd_2Fe_{14}B$ [6]. While in the S30-AsSpun sample the onset temperature of the peak was 554.4 °C. The addition of sulfur slightly changed the crystallization temperature by 5.6°C.

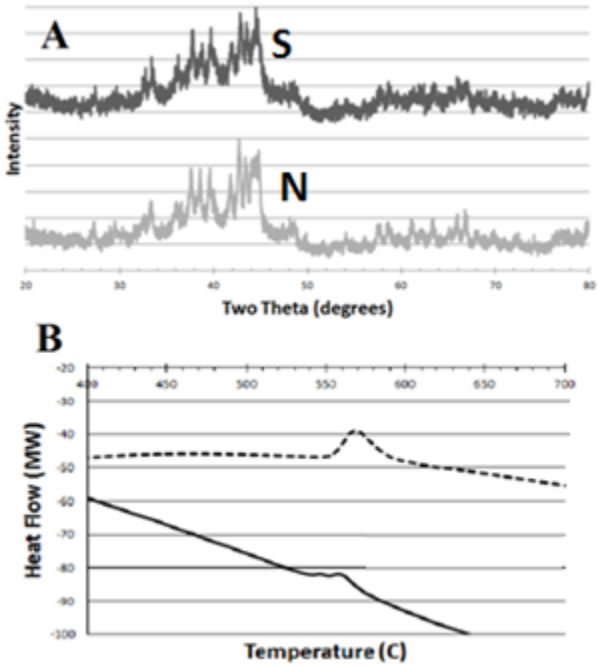

Figure 5.1: A) XRD pattern for the N30 and S30 as spun samples. B) DTA of N30-as-spun (solid) and S30-as-spun (dashed) samples indicating crystallization.

After annealing at either 700 °C or 800 °C and milling for various amounts of time, figures 5.2-5.5 show the X-ray diffraction patterns for all samples. All of the peaks were indexed to the $Nd_2Fe_{14}B$ structure after annealing. Apparently, the sulfur did not alter the phase formation. The trend with respect to milling time was similar for all samples regardless of annealing temperature or sulfur content. Milling resulted in a broadening in the XRD peaks that increased with milling time. This indicates a particle size and/or grain size reduction, showing the longer the sample was milled the smaller the particles or grain size became. One important feature to note is that the broadening seen in the sulfur-modified samples occurred at later milling times, indicating that the grain size was larger in the sulfur-modified samples than in the sulfur-free samples. This could signify that in the sulfur-free samples there is fracture occurring through the grains (transgranular fracture) making them smaller. Even though the peaks were broadened they were still consistent with the $Nd_2Fe_{14}B$ structure, signifying that there was no phase change or oxidation during the milling process. There are no peaks consistent with the Nd-S or Nd_2-S_3 structure which can be representative of two things: there is Nd-S/ Nd_2-S_3 present but in such small quantities that its relative intensity is too small to be seen, or there is no Nd-S present in the material.

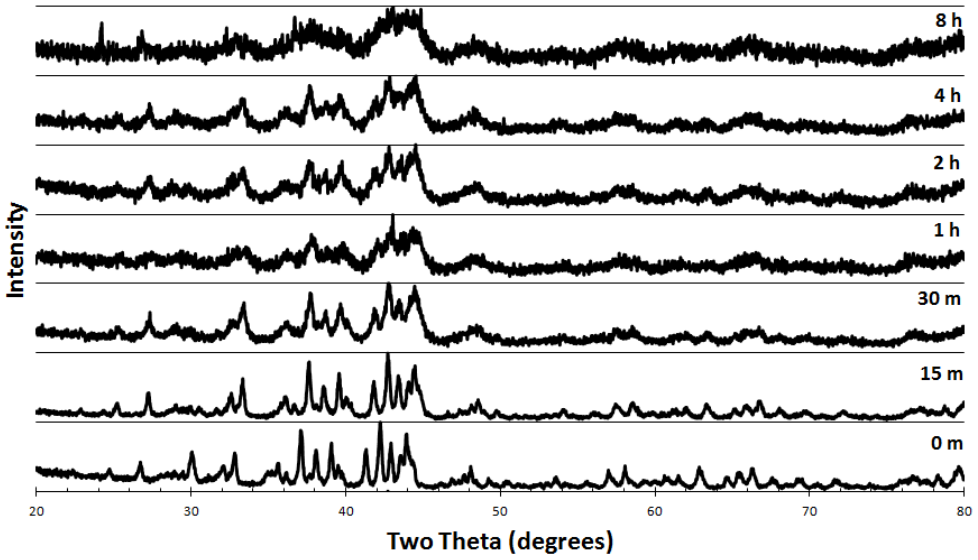

Figure 5.2: X-ray diffraction patterns for the sulfur-free samples annealed at 700 C (N30-700) and milled at various times.

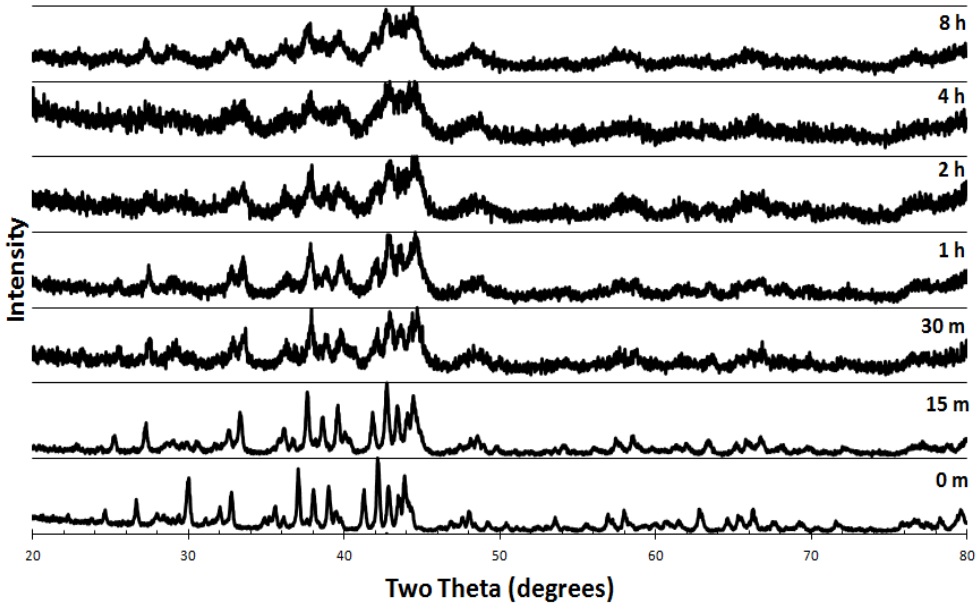

Figure 5.3: X-ray diffraction patterns for the sulfur-free samples annealed at 800 C (N30-800) and milled at various times.

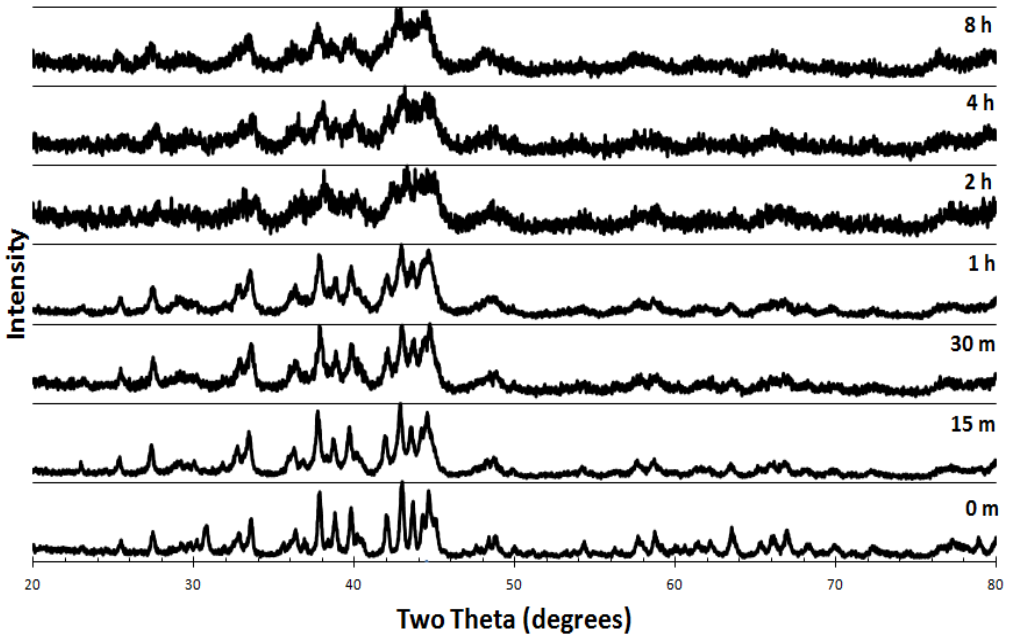

Figure 5.4: X-ray diffraction patterns for the sulfur-modified samples annealed at 700 C (S30-700) and milled at various times.

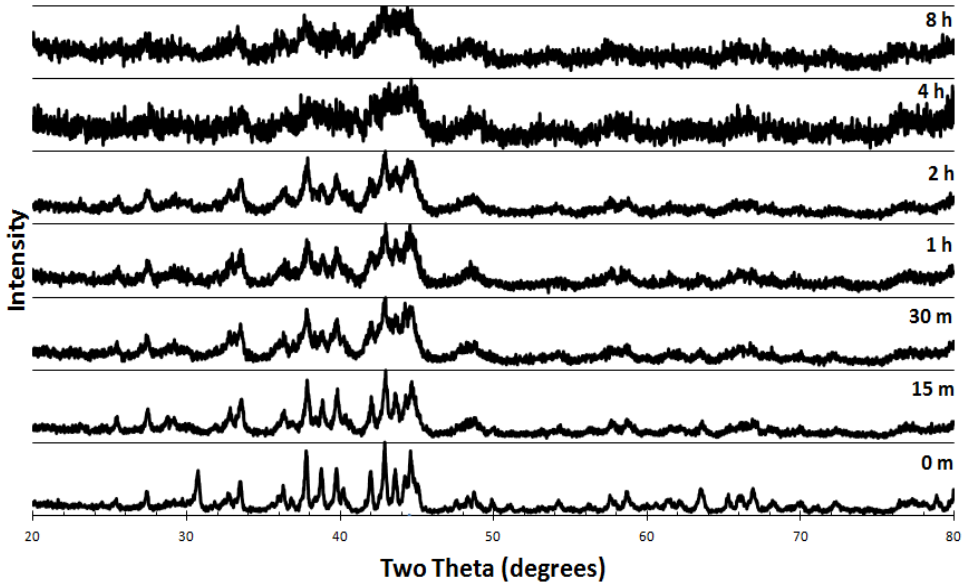

Figure 5.5: X-ray diffraction patterns for the sulfur-modified samples annealed at 800 C (S30-800) and milled at various times.

Scanning electron microscopy (SEM) was used to investigate the particle size and morphology. Figure 5.6 shows SEM micrographs for the samples at milling times of .5 h

minutes, 2, and 8 hours; figure 5.7 shows the graph of the particle size versus milling time.

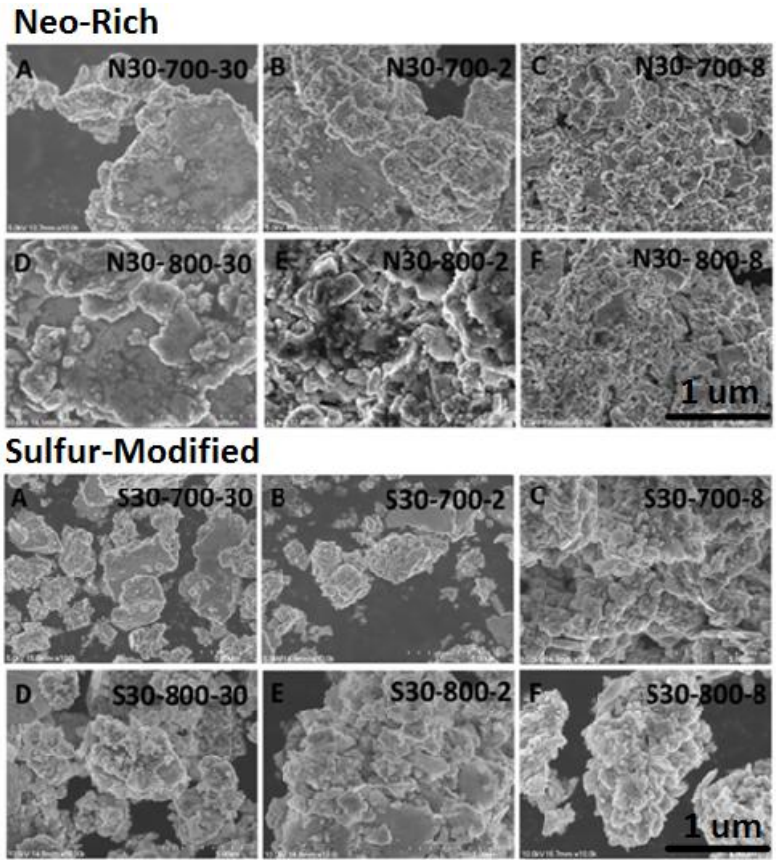

Figure 5.6: SEM images for sulfur-free and sulfur modified samples annealed at 700 C and 800 C.

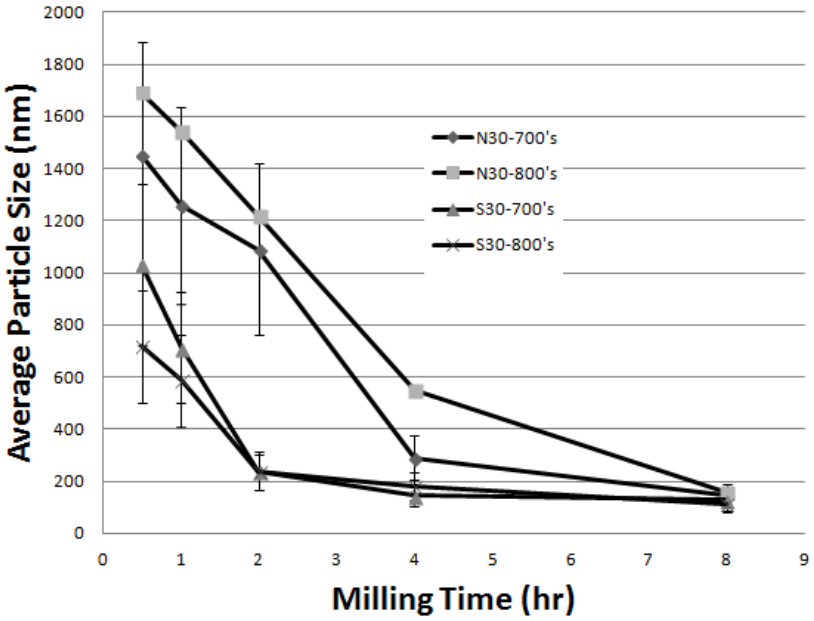

Figure 5.7: Particle size v. milling time of all samples.

Figure 5.7 shows that the particle size of all samples, regardless of annealing time and sulfur content, decreased as milling time increased. However, the sulfur-modified samples showed a quicker progression to smaller particle size. After 30 minutes of milling the sulfur-free samples are approximately twice the size of the sulfur-modified samples. After 8 hours of milling time all of the samples were approximately 150 nm in diameter. The longer the milling the time the more uniform the sample size became. Initially there is a very large error but the error decreases as milling time increases, by 8 hours of milling all samples had the same uniform particle size.

Transmission electron microscopy (TEM) was utilized to investigate the particle size of the samples that were milled for 8 hours. Micrographs of single particles and high resolution images of their lattice fringes were collected. The TEM micrographs were paired with the SEM micrographs of the fresh fracture surfaces of the respective samples that were not milled. Figures 5.8-5.11 show these results.

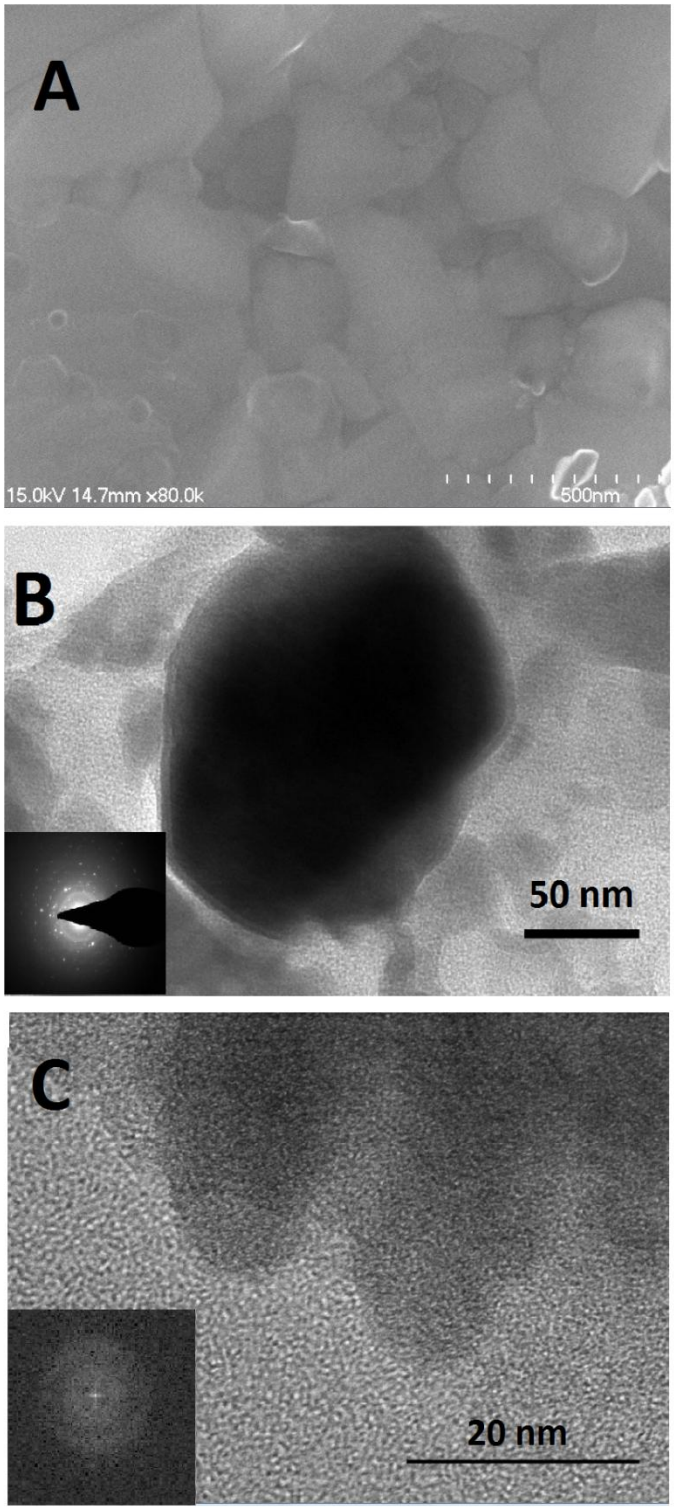

Figure 5.8: A) SEM image of N30-700 sample's fracture surface. B) TEM imaging of single polycrystalline particle found in the N30-700-8 sample. C) TEM imaging of lattice fringes on a polycrystalline particle found in the N30-700-8 sample.

Figure 5.8 shows SEM and TEM micrographs from the N30-700 and N30-700-8 sample. Figure 5.8A shows the SEM images from a fracture surface of the N30-700 sample. The fracture surface is smooth indicating transgranular fracture. Figure 5.8B shows a single particle approximately 150 nm in diameter found in the N30-700-8 sample. The corresponding diffraction pattern shown in the lower left hand corner indicates that the particle is polycrystalline, because the reflections are randomly oriented. Figure 5.8C is a higher magnification image of another particle found in the sample and shows lattice fringes of different orientations. The diffraction pattern in the lower left hand corner also indicates a polycrystalline sample. Thus, after 8 hours of milling the particles in the N30-700-8 sample consist of polycrystalline nanoparticles on the order of 200 nm that formed via transgranular fracture.

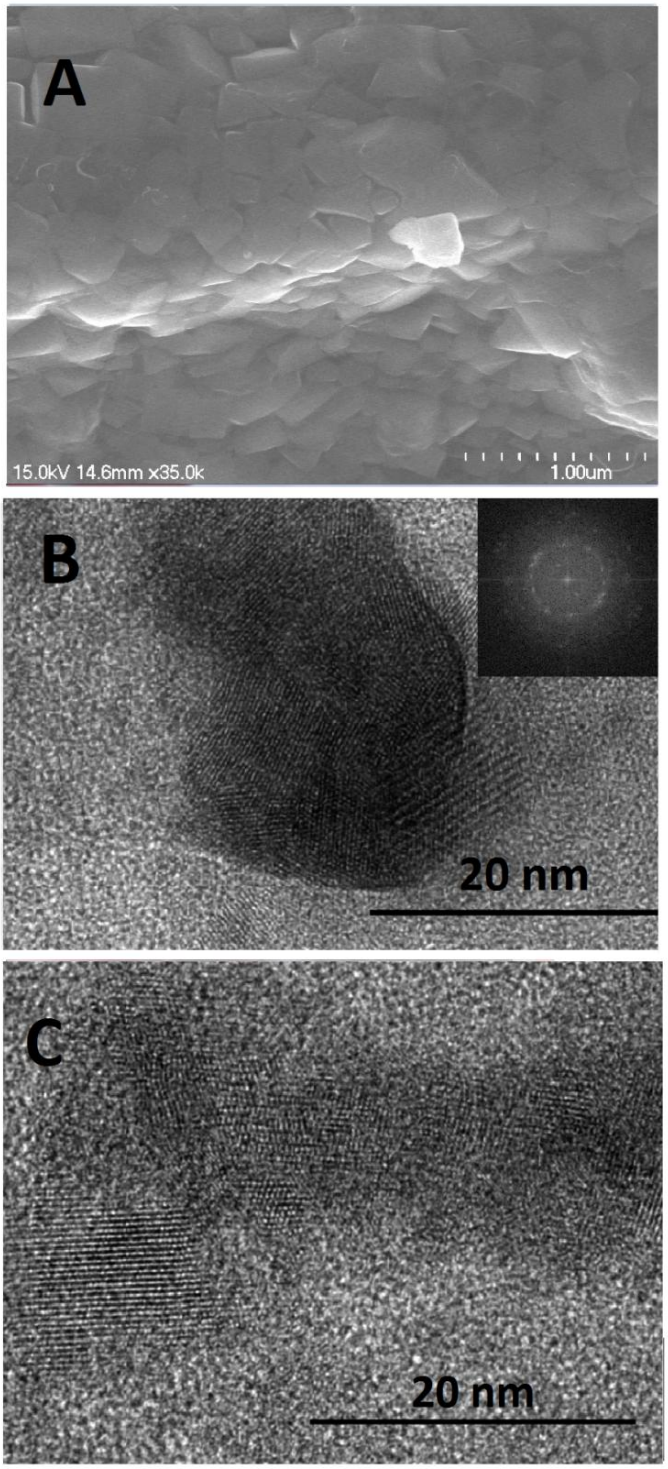

Figure 5.9: A) SEM image of N30-800 sample's fracture surface. B) TEM imaging of single polycrystalline particle found in the N30-800-8 sample. C) TEM imaging of lattice fringes on a polycrystalline particle found in the N30-800-8 sample.

Figure 5.9 is the same series of images from the N30-800 sample. Figure 5.9A is an SEM image showing the fracture surface of the N30-800 sample. Again the fracture surface is smooth indicating transgranular fracture. Figure 5.9B shows a single particle with a diameter of approximately 25 nm from the N30-800-8 sample. The diffraction pattern for this particle, shown in the upper right hand corner, suggests a polycrystalline particle. Figure 5.9C is a higher magnification image of another particle in the N30-800-8 sample where the lattice fringes are clearly visible and have distinctly different orientations, indicative of a polycrystalline particle. Thus, the N30-800-8 samples consist of polycrystalline nanoparticles in the order of 25 nm produced via transgranular fracture.

This data suggests that the particles in the N30-700-8 and N30-800-8 samples are an agglomeration of many different grains that fractured from transgranular breakage and, resulting in polycrystalline nanoparticles.

Figure 5.10, the same series of images but are taken from the S30-700 and S30-700-8 samples. Figure 5.10A is the SEM micrograph showing fracture surface of the non-milled sample. The surface is uneven and irregular, this differs from the smooth fracture surface seen in the sulfur-free samples. The jagged fracture surface indicates intergranular fracture. Figure 5.10B is a TEM image of a single particle with a diameter of approximately 150 nm from the h hour milled sample, which is the same size as the grain size. The diffraction pattern, in the lower left hand corner, indicates a single crystalline particle. Figure 5.10C is a higher magnification image of another particle where the lattice fringes extend across the entire particle, indicating a single crystalline particle.

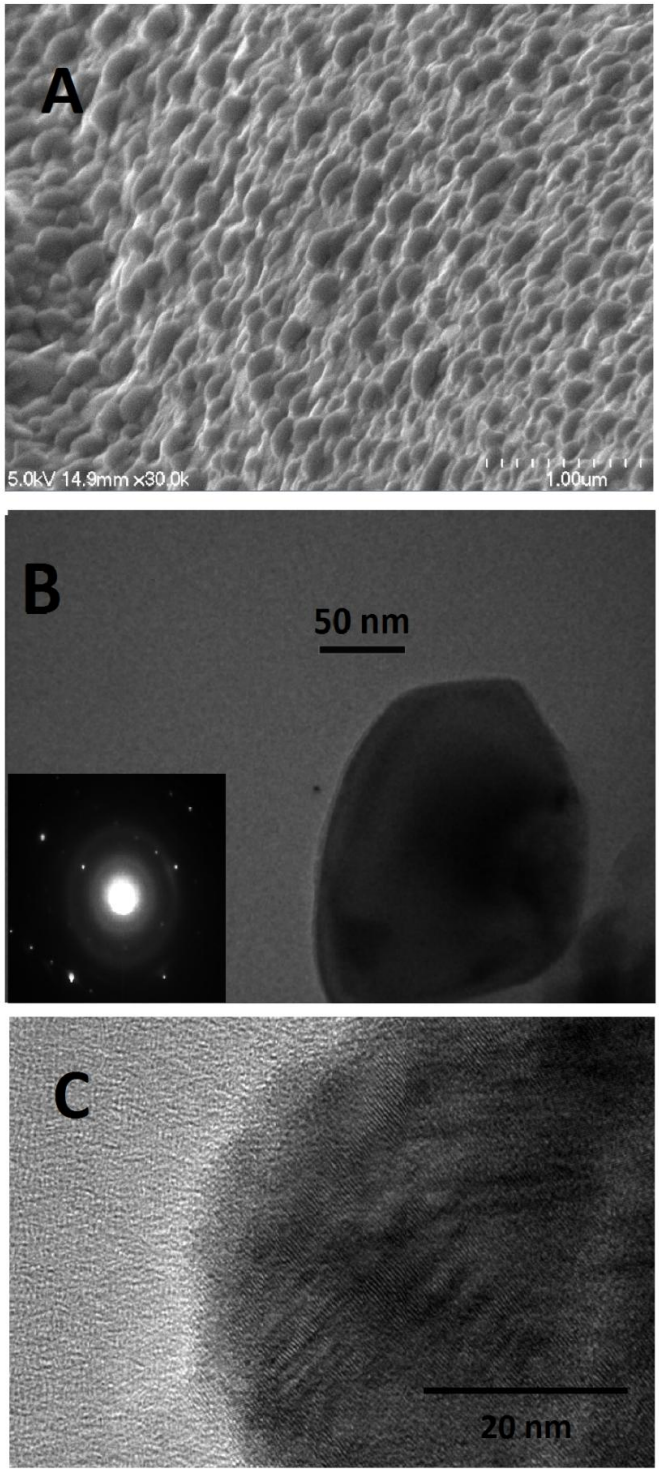

Figure 5.10: A) SEM image of S30-700 sample's fracture surface. B) TEM imaging of a single particle with one crystallographic orientation found in the S30-700-8 sample. C) TEM imaging of lattice fringes across the entire particle found in the S30-700-8 sample.

Figure 5.11 shows micrographs from the S30-800 and S30-800-8 samples. Figure 5.11A is an SEM image from the S30-800 non-milled sample. The fracture surface is uneven and jagged, indicating intergranular fracture; consistent with the S30-700 sample. Figure 5.11B shows a single particle with a diameter of approximately 90 nm from the 8 hour milled sample. The diffraction pattern of the particle shows that it is single crystalline, the reflections are linear and ordered. Figure 5.11C shows the lattice fringes across the entire particle with one orientation, demonstrating a single crystalline particle.

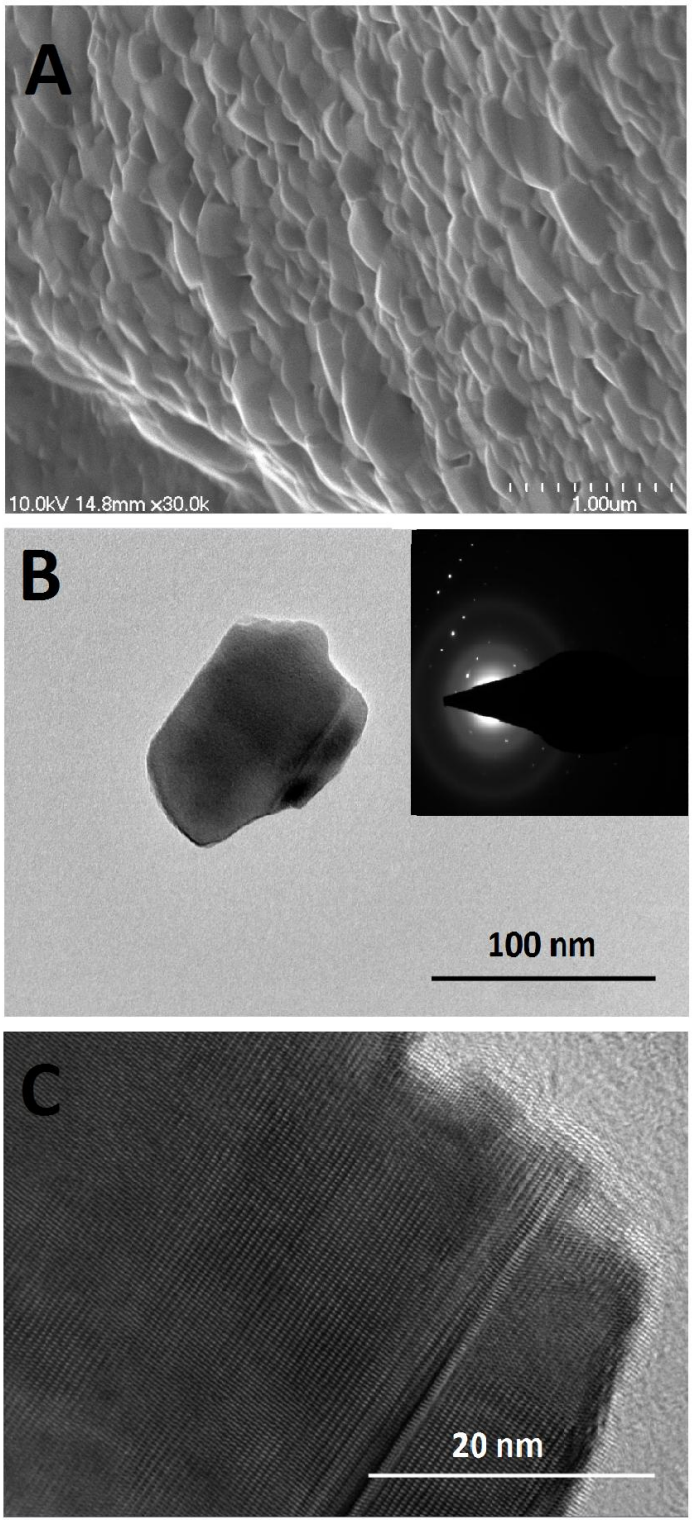

Figure 5.11: A) SEM image of S30-800 sample's fracture surface. B) TEM imaging of single particle with one crystallographic orientation found in the S30-800-8 sample. C) TEM imaging of lattice fringes across the entire particle found in the S30-800-8 sample.

This data suggest that the sulfur-modified alloys experience intergranular fracture during the milling process and did not re-weld during milling. Instead of an agglomeration of polycrystalline particles, which were found in the sulfur-free samples, single crystalline particles were obtained.

The magnetic properties of the samples were also analyzed. Figure 5.12 shows the hysteresis loops for the N30-AsSpun and S30-AsSpun samples. The samples had no remanence and no coercivity, consistent with the XRD and DTA data which revealed mostly amorphous samples. The sulfur-modified sample had a slightly lower magnetization at 7 kOe then the sulfur-free sample.

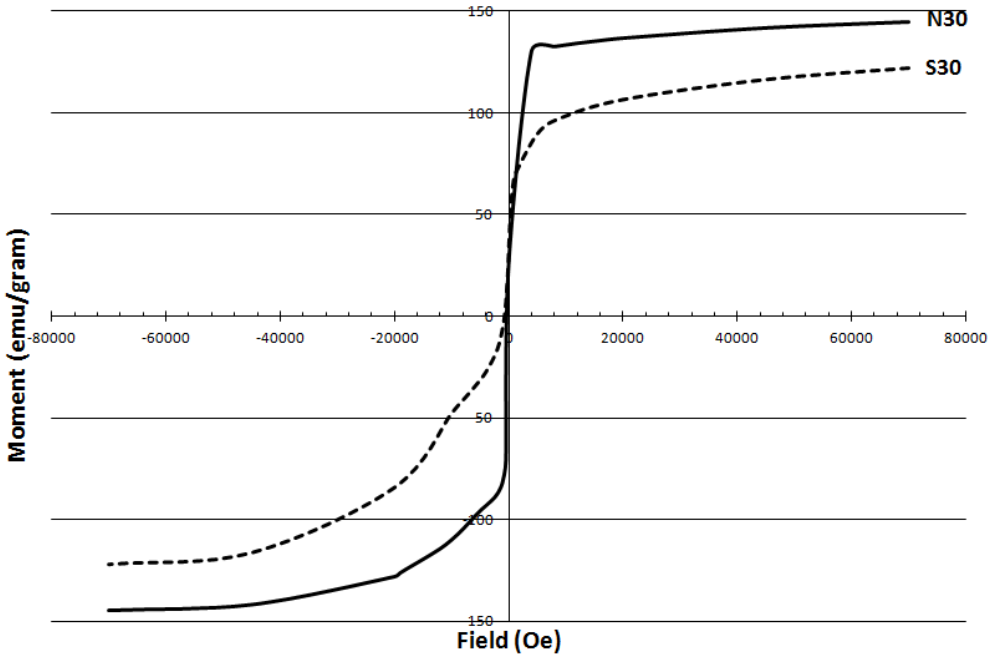

Figure 5.12: Hysteresis loop of the N30-as-spun sample (solid) and the S30-as-spun sample (dashed).

Figures 5.13-5.16 show the second quadrant of the hysteresis loops for the milled samples, showing the remanence and coercivity values. As the milling time increased both the remanence and coercivity decreased, regardless of sulfur content and annealing time.

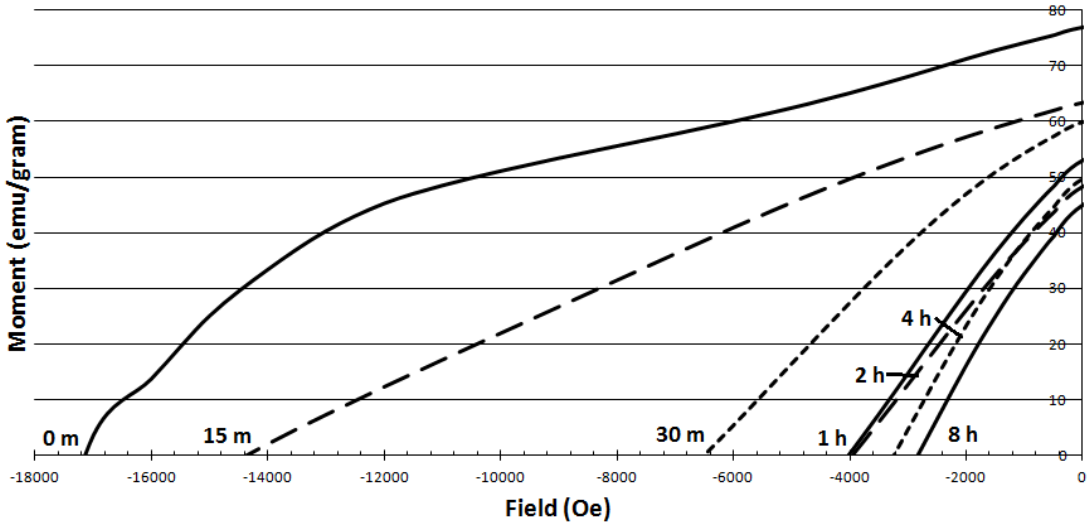

Figure 5.13: Second quadrant of hysterisis loops for all samples annealed at 700 C without sulfur additive.

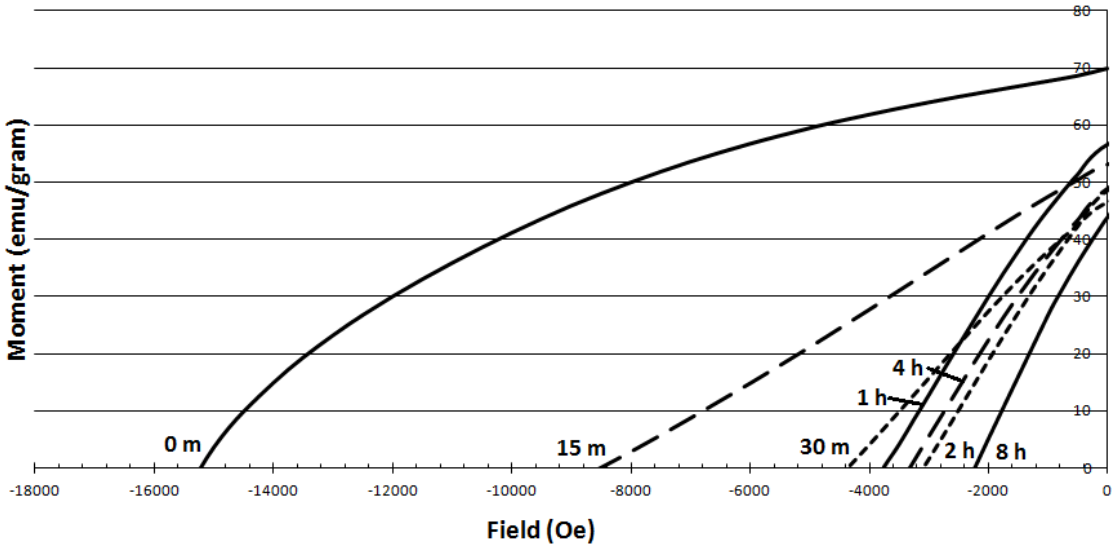

Figure 5.14: Second quadrant of hysterisis loops for all samples annealed at 800 C without sulfur additive.

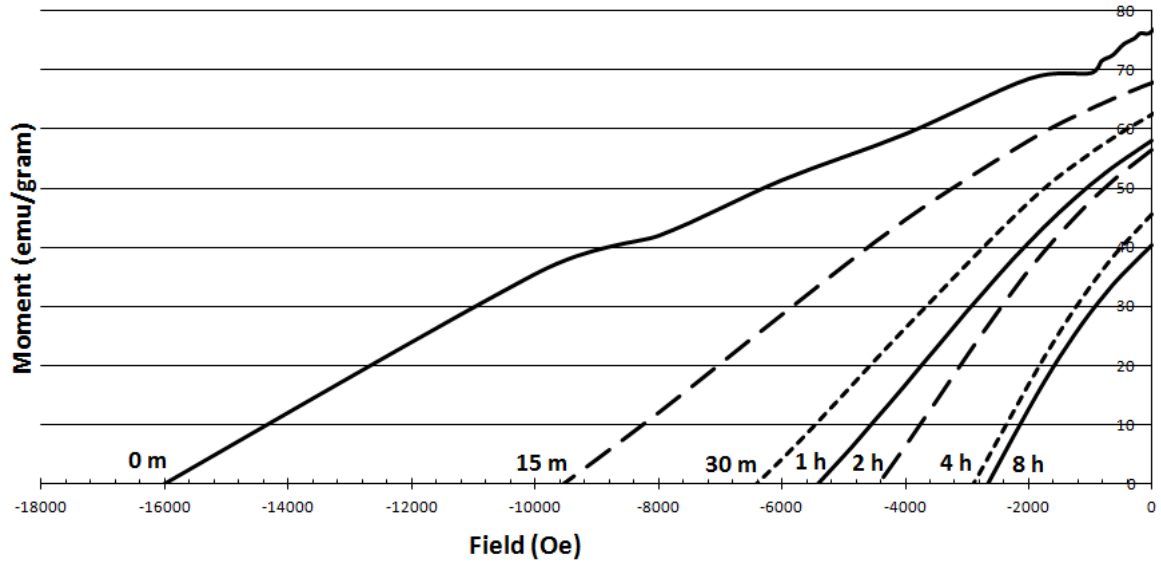

Figure 5.15: Second quadrant of hysterisis loops for all samples annealed at 700 C with the sulfur additive.

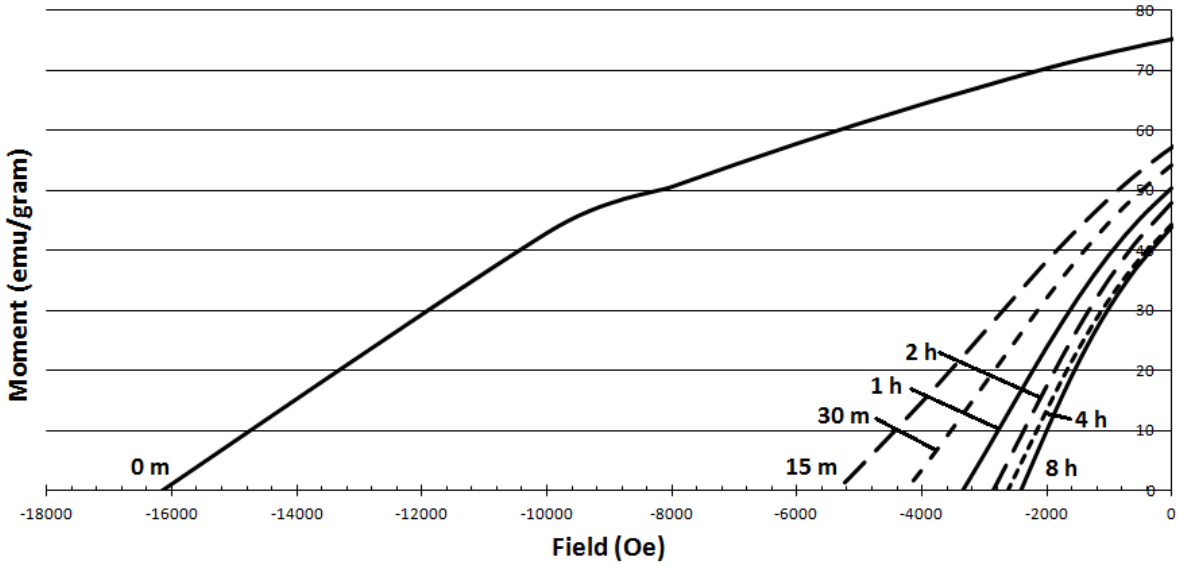

Figure 5.16: Second quadrant of hysterisis loops for all samples annealed at 800 C with sulfur additive.

Figure 5.17 shows the magnetization at 7 kOe for all samples. There is no statistical significance in the difference between the magnetization at7 kOe for the samples, which is anticipated because magnetization is an intrinsic property. The theoretical saturation magnetization for $Nd_2Fe_{14}B$ is 160 emu/g, the experimental values

are slightly lower than this, ranging from 110 – 134 emu/g. This is due to the fact that the samples were not fully saturated. However, these saturation values are consistent with those found experimentally in other surfactant-assisted mechanical milling nanoparticle formation research, which are in the range of 120 emu/g [21]. Figure 5.18 shows that the remanece decreases with additional milling time. After 8 hours of milling the remanence ranged from 40-45 emu/g, which is approximately half of what the theoretical remanence is. Figure 5.19 shows the coervcivity also diminishes with additional milling time. After 8 hours of milling the coercivity ranged from 2.4 – 2.8 kOe. This is slightly lower but in the same range as previous research regarding SA-HEBM nanoparticles, which found the coercivity of nanoparticles to be between 1.2-4 kOe [20,.21]. Figure 5.20 shows the derived energy product, it too decreases with additional milling time. The resultant energy product of the nanoparticles was in the range of 1.7 – 2.1 MGOe.

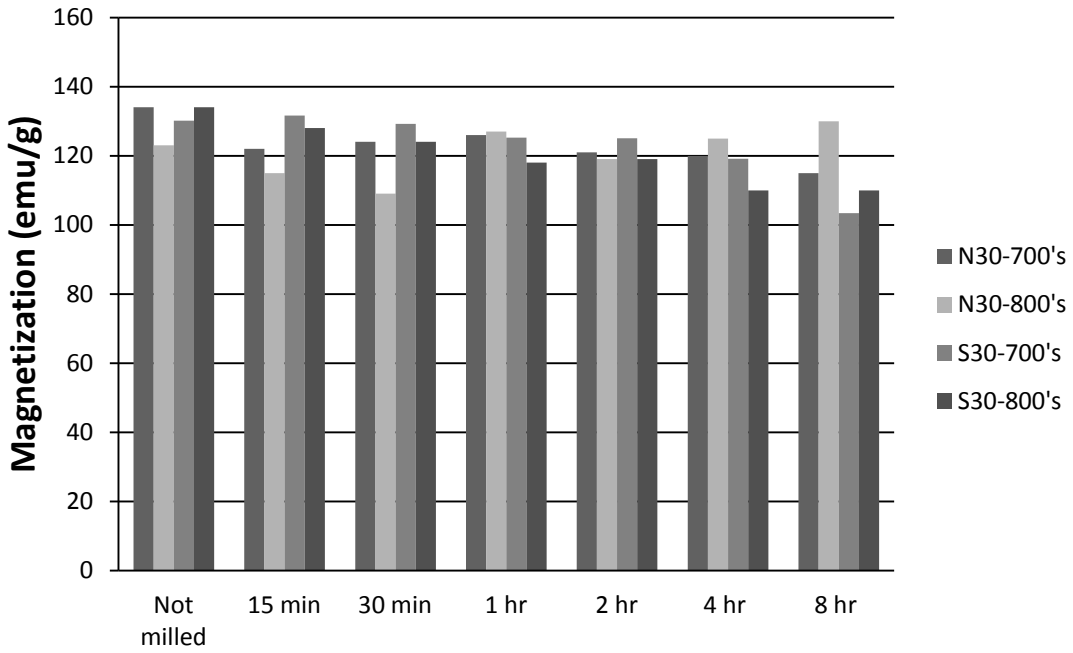

Figure 5.17: Summary of magnetization at 7 kOe of all samples.

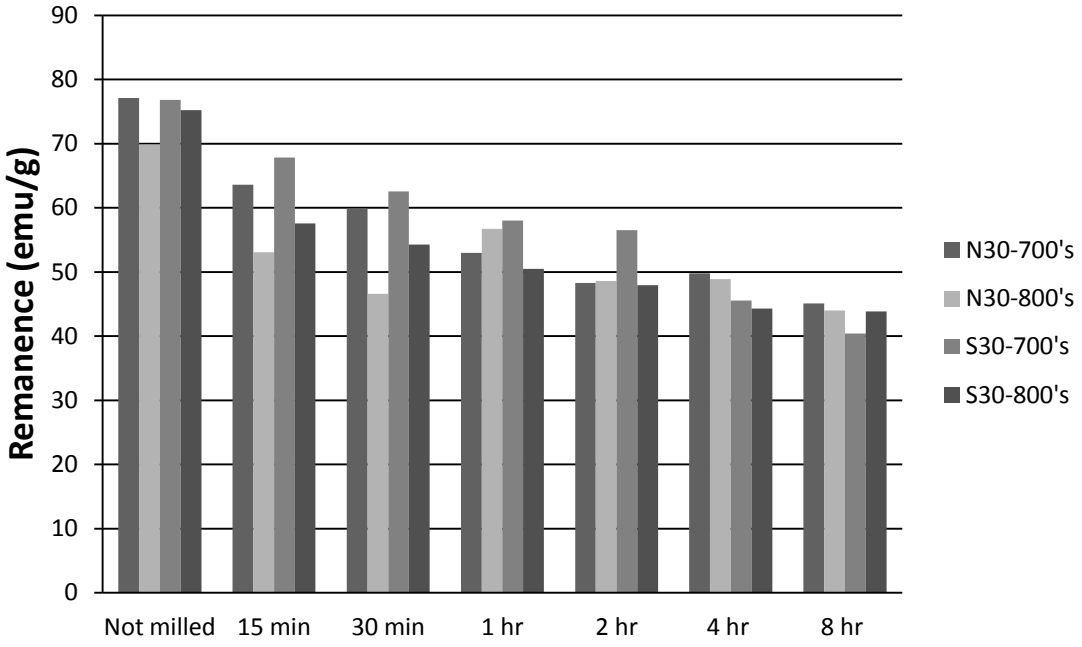

Figure 5.18: Summary of remanence of all samples.

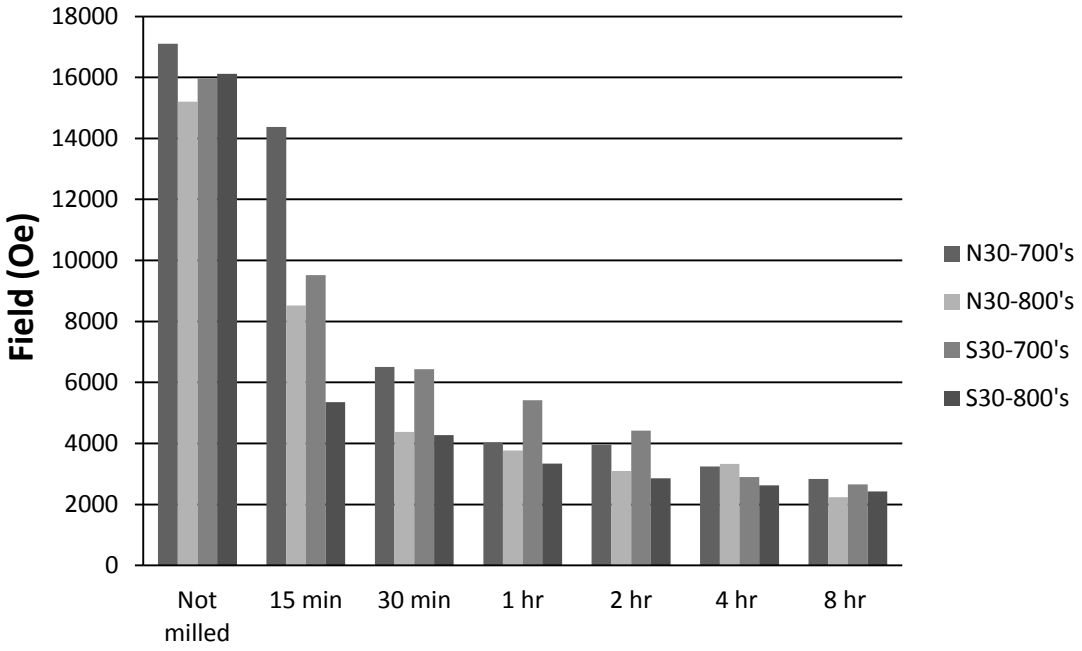

Figure 5.19: Summary of the coercivity of all samples.

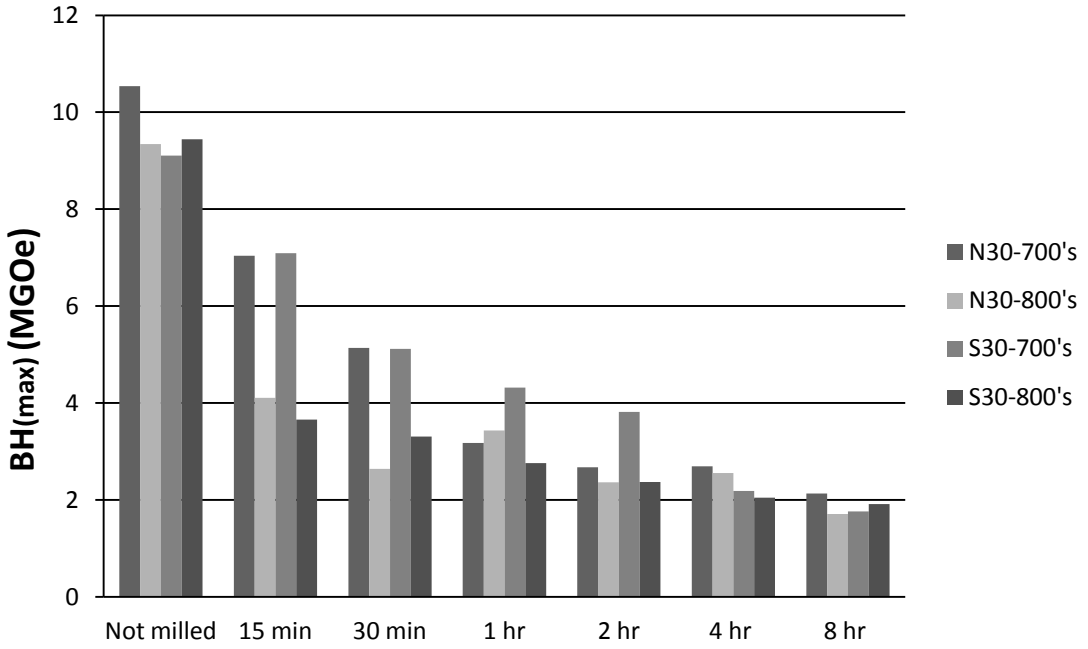

Figure 5.20: Summary of the energy product of all samples.

The magnetic properties were not improved by the milling process. The same trends were seen in all samples. A larger initial loss in both remanence and coercivity was seen in the samples that were annealed at 800 °C, than was seen in the samples that were annealed at 700 °C. However, the reduction in both coercivity and remanence was the same for both annealing temperatures by a milling time of 1 hour and similar losses after that point were experienced by all samples. Regardless of annealing temperature and sulfur content, the samples experienced the same overall loss in magnetic properties.

Chapter 6 Conclusions

Nd-rich $Nd_2Fe_{14}B$ permanent magnets and sulfur-modified $Nd_2Fe_{14}B$ permanent magnets were prepared and analyzed. The SEM imaging showed a smooth fracture surface for the sulfur-free samples and an uneven fracture surface for the sulfur-modified samples. This indicates that the addition of sulfur aided in altering the fracture behavior from transgranular fracture to intergranular fracture. The sulfur successfully acted as an embrittlement agent and forced fracture along the grain boundaries instead of through the grain boundaries as seen in the sulfur free samples.

Further evidence of the change in fracture behavior was seen in the TEM images. The sulfur free samples diffraction patterns indicated they were polycrystalline, and images of the lattice fringes verify this finding. In the case of the sulfur-modified samples, the particles were single crystalline as indicated by the diffraction patterns and verified by images of the lattice fringes. The particle size in the sulfur-modified samples was consistent with the grain size in the initial samples. Indicating the fracture behavior was modified to intergranular fracture, consistent with the SEM images.

Even though the fracture behavior was successfully modified and single grain nanoparticles were fabricated, the fabrication of these nanoparticles did not aid in the enhancement of magnetic properties. The magnetization at 7 kOe was consistent at approximately 120 emu/g, there was a decrease in both remanence and coercivity, resulting in values in the range of 45 emu/g, and 2.7 kOe respectively. These decreases resulted in energy products around 2 MGOe.

References

1) Permanent Magnet Applications Guide. 2013 Arnold Magnetic Technologies. http://www.arnoldmagnetics.com/Permanent_Magnet_Applications_Guide.aspx
2) Sustainable Energy. Magnet Energy. http://www.magnetnrg.com/pm-history.html
3) M. Sagawa, S. Hirosawa, H. Yamamoto, S. Fujimura, Y. Matsuura: Jpn . J Appl. Phys. 26 (1987) 799
4) O. Gutfleisch, M. Willard, E. Bruck, C. Chen, S. Sankar, J. Ping Lu: Adv. Materials. 2010. 3
5) N. Jones: Nature. 472 (2011) 22
6) Coey, J. (2010). *Magnetism and Magnetic Materials*. Dublin: Cambridge University Press
7) Catherine Westbrook, Carolyn Kaut, Carolyn Kaut-Roth (1998). *MRI (Magnetic Resonance Imaging) in practice* (2 ed.). Wiley-Blackwell. p. 217. ISBN 0-632-04205-2.
8) Ashcroft, Neil W.; Mermin, N. David (1977). *Solid state physics* (27. repr. ed.). New York: Holt, Rinehart and Winston. ISBN 978-0-03-083993-1.
9) The Free Dictionary. Hysteresis. Farlex Inc. 2013. http://encyclopedia2.thefreedictionary.com/Hysteresis
10) Leibniz Institute for Solid State and Materials Research Dresden. Permanent Magnets. http://www.ifw-dresden.de/index.php?id=485&L=0
11) R. Skomski, J.M.D. Coey: IEEE Trans. on Mag. 29 (1993) 2860
12) R. Fischer, T. Schrefl, H. Kronmuller, J. Fidler: J. of Magnetism and Magnetic Materials. 150 (1995) 343
13) D. Brown, B. Ma, Z. Chen: J. of Magnetism and Magnetic Materials. 248 (2002) 432.
14) F. Pinkerton, D.J. Van Wingerden: J. of Appl. Phys. 60 (1986) 3690
15) R. Coehoorn, D.B. De Mooij, C. De Waard: J. of Magnetism and Magnetic Materials. 80 (1989) 101
16) A. Manaf, P.Z. Zhang, I. Ahmad, H.A. Davies and R.A. Buckley. IEEE Trans. On Mag. 29 (1993) 2866
17) I. Ahmad, H.A. Davies, R.A. Buckley. J. of Magnetism and Magnetic Materials: 157/158 (1996) 31-32
18) R. Fischer, T. Schrefl, H. Kronmuller, J.Fidler. J. of magnetism and magnetic materials: 153 (1996) 35
19) J.I. Betancourt, H.A. Davies, J. of Magnetism and Magnetic Materials: 246 (2002) 6-9
20) Q. F. Xiao, T. Zhao, Z.D. Zhang, E. Bruck, K.H.J Buschow, F.R. de Boer. J. of Magnetism and Magnetic Materials: 223 (2001) 215
21) T. Harada, T. Kuji. J. of Appl. Phys: 72 (1992) 5443
22) D. Sellmyer. J. of Appl. Phys. 105 (2009) 07A710.
23) N. Poudyal, C. Rong, J. Ping Liu. J. of Appl. Phys. 107 (2010) 09A703.

24) N. Poudyal, V. Nguyen, C. Rong, J. Ping Liu. J of Phys. D: Appl. Phys. 44 (2011) 335002
25) N. Akdogan. G. Hadjipanayis. D. Sellmyer. Nanotechnology: 21 (2010) 295705
26) K P Su, Z W Liu, D C Zeng, D X Huo, L W Li, G Q Zhang. J. of Phys. D. Appl. Phys.46 (2013) 245003 (5pp)
27) B.Z. Cui, L.Y. Zheng, W.F. Li, J.F. Liu, G.C. Hadjipanayis. Acta Materialia 60 (2012) 1721-1730
28) Callister, William D. Materials Science and Engineering an Introduction. New York : Von Hoffman Press, 2002. pp. 673-700. Vol. 11.
29) Sagawa, Masato, et al. "Nd-Fe-B Permanent Magnet Materials." *Japanese Journal of Applied Physics* 26.6 (1987): n. pag. Print.
30) Magnetic Spectroscopy of Fundamental Materials. Daniel Haskel. Argonne National Laboratory. 2007. http://www.aps.anl.gov/~haskel/UCReview-DH.pdf
31) Raghavan, V. B-Fe-Nd (Boron-Iron_Neodymium). 2003, Vol. 24, 5.
32) Nanocomposite Permanent Magnets. Jeff Shield. 2013 NCMN. http://www.unl.edu/ncmn/research/nanocomposite_permanent_magnets.shtml
33) Cullity, B. D., and S. R. Stock. *Elements of X-ray Diffraction*. Third ed. New Jersey: Prentice Hall,2001. Print.
34) OpenStax College. (2013, September 11). *Photon Energies and the Electromagnetic Spectrum*. Retrieved from the Connexions Web site: http://cnx.org/content/m42563/1.7/3
35) Geochemical Instrumentation and analysis. Scanning Electron Microscope. 2013. http://serc.carleton.edu/research_education/geochemsheets/techniques/SEM.html
36) Radiological and Environmental Management. Scanning Electron Microscope. Purdue University 2010. http://www.purdue.edu/rem/rs/sem.htm
37) The Transmission Electron Microscope. Nobel Media AB 2013. http://www.nobelprize.org/educational/physics/microscopes/tem/
38) NCMN Electron Microscopy. TEM. University of Nebraska 2013. http://ncmn.unl.edu/cfem/microscopy/TEM.shtml
39) McElfresh, M. (1994). *Fundamentals of Magnetism and Magnetic Measurements: Featureing Quantum design magnetic measurement system*. Quantum Design.